Regional inversion shows promise in capturing extreme-event-driven CO2 flux anomalies but is limited by atmospheric CO2 observational coverage

Brendan Byrne[1], Junjie Liu[2], Kevin W. Bowman[3], Yi Yin[4], Jeongmin Yun[5], Gabriel Ferreira[6], Stephen Ogle[6], Latha Baskaran[7], Liyin He[8], Xing Li[9], Jingfeng Xiao[10], and Kenneth J. Davis[11]

[1]Jet Propulsion Lab
[2]Jet Propulsion Laboratory
[3]Jet Propulsion Lab (NASA)
[4]New York University
[5]NASA Jet Propulsion Laboratory
[6]Colorado State University
[7]Jet Propulsion Laboratory, California Institute of Technology
[8]Carnegie Institution for Science
[9]Seoul National University
[10]University of New Hampshire
[11]Pennsylvania State University

September 30, 2023

Abstract

Extreme climate events are becoming more frequent, with poorly understood implications for carbon sequestration by terrestrial ecosystems. A better understanding will critically depend on accurate and precise quantification of ecosystems responses to these events. Taking the 2019 US Midwest floods as a case study, we investigate current capabilities for tracking regional flux anomalies with "top-down" inversion analyses that assimilate atmospheric CO2 observations. For this analysis, we develop a regionally nested version of the NASA Carbon Monitoring System-Flux (CMS-Flux) that allows high resolution atmospheric transport ($0.5° \times 0.625°$) over a North America domain. Relative to a 2018 baseline, we find US Midwest growing season net carbon uptake is reduced by 11-57 TgC (3-16%) for 2019 (inversion mean estimates across experiments). These estimates are found to be consistent with independent "bottom-up" estimates of carbon uptake based on vegetation remote sensing. We then investigate current limitations in tracking regional carbon emissions and removals by ecosystems using "top-down" methods. In a set of observing system simulation experiments, we show that the ability to recover regional carbon flux anomalies is still limited by observational coverage gaps for both in situ and satellite observations. Future space-based missions that allow for daily observational coverage across North America would largely mitigate these observational gaps, allowing for improved top-down estimates of ecosystem responses to extreme climate events.

Regional inversion shows promise in capturing extreme-event-driven CO_2 flux anomalies but is limited by atmospheric CO_2 observational coverage

B. Byrne[1], J. Liu[1,2], K. W. Bowman[1,3], Y. Yin[2,*], J. Yun[1], G. D. Ferreira[4], S. M. Ogle[4,5], L. Baskaran[1], L. He[6], X. Li[7], J. Xiao[8], K. J. Davis[9]

[1]Jet Propulsion Laboratory, California Institute of Technology, Pasadena, CA, USA
[2]Division of Geological and Planetary Sciences, California Institute of Technology, Pasadena, CA, USA
[3]Joint Institute for Regional Earth System Science and Engineering, University of California, Los Angeles, USA
[4]Natural Resource Ecology Laboratory, Colorado State University, Fort Collins, CO 80523, United States of America
[5]Department of Ecosystem Science and Sustainability, Colorado State University, Fort Collins, CO 80523, United States of America
[6]Department of Global Ecology, Carnegie Institution for Science, Stanford, CA, United States of America
[7]Research Institute of Agriculture and Life Sciences, Seoul National University, Seoul, South Korea
[8]Earth Systems Research Center, Institute for the Study of Earth, Oceans, and Space, University of New Hampshire, Durham, NH, USA
[9]Department of Meteorology and Atmospheric Science, and Earth and Environmental Systems Institute, The Pennsylvania State University, University Park, Pennsylvania
[*]Now at Department of Environmental Studies, New York University, New York, NY, USA

Key Points:

- Bottom-up and top-down methods independently capture reduced 2019 US Midwest carbon uptake
- Gaps in atmospheric CO_2 observations drive uncertainties in top-down estimates
- Nested inversion better localizes US Midwest ΔNEE relative to coarse global model

Corresponding author: Brendan Byrne, `brendan.k.byrne@jpl.nasa.gov`

Corresponding author: Junjie Liu, `junjie.liu@jpl.nasa.gov`

Abstract

Extreme climate events are becoming more frequent, with poorly understood implications for carbon sequestration by terrestrial ecosystems. A better understanding will critically depend on accurate and precise quantification of ecosystems responses to these events. Taking the 2019 US Midwest floods as a case study, we investigate current capabilities for tracking regional flux anomalies with “top-down” inversion analyses that assimilate atmospheric CO_2 observations. For this analysis, we develop a regionally nested version of the NASA Carbon Monitoring System-Flux (CMS-Flux) that allows high resolution atmospheric transport ($0.5°\times0.625°$) over a North America domain. Relative to a 2018 baseline, we find US Midwest growing season net carbon uptake is reduced by 11-57 TgC (3–16%) for 2019 (inversion mean estimates across experiments). These estimates are found to be consistent with independent “bottom-up” estimates of carbon uptake based on vegetation remote sensing. We then investigate current limitations in tracking regional carbon emissions and removals by ecosystems using “top-down” methods. In a set of observing system simulation experiments, we show that the ability to recover regional carbon flux anomalies is still limited by observational coverage gaps for both in situ and satellite observations. Future space-based missions that allow for daily observational coverage across North America would largely mitigate these observational gaps, allowing for improved top-down estimates of ecosystem responses to extreme climate events.

Plain Language Summary

Extreme climate events, such as floods or heatwaves, can have major impacts on the carbon cycle. For example, widespread flooding in the US Midwest during 2019 delayed the planting of crops leading to reduced plant growth and carbon uptake relative to 2018. Here, we test how well this reduction in carbon uptake can be inferred from measurements of atmospheric CO_2. We find that these data can identify reduced net carbon uptake to the US Midwest during the 2019 floods, but that sparse observational coverage limits our ability to quantify the anomaly in net carbon uptake.

1 Introduction

Extreme events, including heat and precipitation extremes, are becoming more frequent (Shenoy et al., 2022; Q. Sun et al., 2021; Kirchmeier-Young & Zhang, 2020; Seneviratne et al., 2021). These events have significant implications for carbon sequestration in terrestrial ecosystems, often causing carbon losses in a single year equal to many years of carbon sequestration (Ciais et al., 2005; Byrne et al., 2021). This is concerning because Nature-based Climate Solutions (NbCSs), which aim to enhance the terrestrial carbon sink through improved land management, have been proposed as an important tool to mitigate CO_2 emissions (Fargione et al., 2018). The increasing frequency of extreme events may disrupt this process, creating a carbon-climate feedback where extreme-event-driven carbon emissions reduce the effectiveness of NbCSs (Zscheischler et al., 2018; Barkhordarian et al., 2021). Consequently, there is an urgent need to quantify the impact of extreme events on carbon uptake by ecosystems for policy programs and other climate applications.

“Top-down” methods offer an approach for estimating biosphere-atmosphere CO_2 fluxes based on observations of atmospheric CO_2. Typically, Bayesian inverse methods are used to estimate optimal surface fluxes based on constraints from prior information and atmospheric CO_2 observations. Although historically data limited, these techniques are increasingly used to quantify regional carbon cycle responses to extreme events, thanks to expansions of in situ CO_2 measurements and the introduction of space-based retrievals of column-averaged dry-air CO_2 mole fractions (X_{CO_2}) from missions like the Orbiting Carbon Observatory 2 (OCO-2) (Feldman et al., 2023; Byrne et al., 2021). Still, current capabilities for tracking extreme events are not well understood. This study aims to improve our characterization of these capabilities and identify current limitations.

As a case study, we examine the 2019 US Midwest floods. Intense precipitation during that spring ($> 2\sigma$ above average) led to widespread flooding across the US Midwest, a region that accounts for 40% of world corn and soybean production (Yin et al., 2020). Inundation delayed crop planting by 2–3 weeks relative to 2018 across the region, with an additional reduction of 6.8 million hectares in the total planted area. These factors led to a 16-day shift in the seasonal cycle of photosynthesis relative to 2018, along with a 15% lower peak value (Yin et al., 2020). In turn, crop yields across the US Midwest were reduced by $\sim$14%, and a decrease in net carbon uptake of $\sim$0.1 PgC was inferred relative to the preceding years (Yin et al., 2020; Balashov et al., 2022). The relatively simple (delayed planting) and well documented carbon cycle perturbation during this event makes it an ideal case study for studying our ability to quantify carbon cycle perturbations using top-down and bottom-up methods.

To perform our analysis, we introduce a regionally nested version of the CMS-Flux inversion system with high-resolution ($0.5°\times0.625°$) atmospheric transport over North America (see Sec. 2.1). This version offers advantages over the coarse-resolution ($4°\times 5°$) global version of CMS-Flux. It reduces transport errors introduced by the coarsening of reanalysis winds (Stanevich et al., 2020; K. Yu et al., 2018) and better represents assimilated CO_2 observations, resulting in improved localization of extreme-event-driven CO_2 flux anomalies (Sec. 3.2.2).

The first objective of this study is to evaluate how well existing atmospheric observing systems can quantify flood-induced reductions in carbon uptake during 2019 relative to 2018. We conduct four inversions that assimilate (1) in situ CO_2 measurements (IS), (2) OCO-2 land X_{CO_2} retrievals (LNLG), (2) both insitu and OCO-2 land data (LNLGIS), or (4) in situ, OCO-2 land and ocean data (LNLGOGIS)(Sec. 2.1). Climatological prior fluxes are employed in each experiment, allowing us to attribute posterior anomalies in carbon uptake between years solely to the assimilation of atmospheric CO_2 data. We then compare these estimates with an independent ensemble of remote-sensing bottom-up estimates and with crop-yield data to assess their overall consistency (Sec. 3.1).

The second objective of this study is to assess the impact of existing observational coverage gaps and the potential expansion of space-based X_{CO_2} measurements on our ability to detect extreme-event-driven anomalies in CO_2 fluxes. To evaluate the effect of expanded space-based observations, we devise a hypothetical observing system that provides daily X_{CO_2} retrievals at 13:00 local time (similar to OCO-2). Subsequently, we conduct observing system simulation experiments (OSSEs) for existing in situ data and OCO-2 data as-well as the hypothetical observing system. For each OSSE, we evaluate the effectiveness in capturing extreme-event-driven CO_2 flux anomalies (Sec. 3.2.1). Our aim is to gain a deeper understanding of how observational coverage impacts our ability to quantify the influence of extreme events on CO_2 fluxes.

2 Methods

Sec. 2.1 introduces the configuration for the nested North America version of the CMS-Flux atmospheric CO_2 inversion system, including its application for real data experiments (Sec. 2.1.1) and OSSEs (Sec. 2.1.2). Sec. 2.2 describes remote-sensing bottom-up NEE anomaly estimates used in this study. Sec. 2.3 describes the state crop production estimates.

2.1 Top-down ΔNEE estimate

We establish a one-way nested inversion system covering the North America region, spanning from 40°W to 167.5°W and 14°N to 76°N. Within this domain, model transport is conducted at a spatial resolution of 0.5° × 0.625° with a five-minute timestep, using archived MERRA-2 reanalysis data. We employ four-dimensional variational data assimilation (4D-Var) to optimize scaling factors on prior land and ocean fluxes. These fluxes are optimized at a coarser spatial and temporal resolution compared to the nested model transport. Spatially, a mask is applied to optimize fluxes over a 4°×5° grid, which is truncated at the land-ocean boundary. Temporally, we utilize a six-week inversion window and optimize weekly mean land and ocean scaling factors. The middle four weeks of the inversion window are retained as optimized fluxes, while the first and last weeks are excluded as spin-up and spin-down periods. We conduct a batch of eight six-week inversions offset by four weeks, yielding continuous fluxes from April 8th to November 18th for both 2018 and 2019, resulting in a total of 16 inversion runs.

For each experiment, the nested inversion setup is run three times using different prior fluxes (the BCs and ICs also differ for the real-data experiments, see Sec. 2.1.1). The prior NEE fluxes are derived from the posterior NEE fluxes of the GOSAT+surface+TCCON experiment by Byrne et al. (2020) and differ based on the employed prior NEE (CASA, SiB3, or FLUXCOM). A climatological seasonal cycle is calculated for each prior NEE flux over the period of 2010-2015. Subsequently, the climatological NEE seasonal cycle is partitioned into net primary production (NPP) and heterotrophic respiration (HR) components by subtracting the 2010-2015 mean seasonal cycle from the mean bottom-up NPP estimate (assumed to be 65% of mean GPP estimate here). In the inversions, we impose both the NPP and HR fluxes in the forward simulation, but optimize scaling factors only on the weekly mean HR fluxes. This choice is driven by the improved performance of this configuration during the spring and fall when NEE is close to zero, requiring large scaling factors to adjust the NEE flux. The posterior HR fluxes are not interpreted independently but combined with the prior NPP fluxes to obtain a posterior estimate of NEE for analysis. We generate prior uncertainties on the HR fluxes based on the full range of the three prior NEE fluxes. Prior ocean fluxes are derived similarly from the posterior ocean flux estimates of the GOSAT+surface+TCCON experiment by Byrne et al. (2020), and uncertainties on these estimates reflect the range among the three experiments that employ different NEE priors. The prior fluxes, posterior fluxes, and associated uncertainties are provided as supporting information.

In addition to the ocean, NPP, and HR fluxes, the forward simulations incorporate prescribed fossil fuel emissions, biomass burning emissions, biofuel emissions, and diurnal NEE. Fossil Fuel emissions used here were specifically made for the v10 OCO-2 modelling intercomparison project (MIP) (Byrne et al., 2023; Basu & Nassar, 2021). Biomass burning emissions are derived from the Global Fire Emissions Database version 4 (GFED4.1s) and scaled to incorporate diurnal variations in emissions (van der Werf et al., 2017). Biofuel emissions are obtained from the CASA-GFED4-FUEL dataset. Diurnal variations in NEE are based on the diurnal NEE variations from the CASA and SiB3 models, as described in Byrne et al. (2020). The SiB3 diurnal cycle is employed for the SiB3-based and FLUXCOM-based NEE priors, while the CASA diurnal cycle is prescribed for the CASA-based inversion. All of these fluxes are regridded from their native spatial resolution to 0.5°×0.625° (fossil fuel emissions were at 1.0°×1.0° degrees, biomass burning emissions were at 0.25°×0.25° degrees, and remaining fluxes were at 4° × 5° as archived by Byrne et al. (2020)).

2.1.1 Real data experiment

First, we require atmospheric CO_2 boundary and initial conditions for the nested model. To generate these conditions, we conduct a global 4°×5° 4D-Var inversion that optimizes scaling factors on prior land and ocean fluxes. These global inversions utilize the same configuration as Byrne et al. (2020). The resulting optimized global NEE and ocean fields are then employed in a 2°×2.5° global simulation to produce boundary conditions and initial conditions for the nested domain. The global inversions are performed three times, corresponding to each of the three prior NEE estimates. The nested inversion setup is subsequently executed three times using the three different prior fluxes, boundary conditions, and initial conditions based on the three distinct prior flux estimates.

Four sets of experiments are conducted, differing in the assimilated data. The "IS" experiment assimilates in situ CO_2 measurements from the global network of sites as described below. The "LNLG" experiment assimilates OCO-2 land data, including nadir and glint retrievals. The "LNLGIS" experiment assimilates both in situ and OCO-2 land data. Lastly, the "LNLGOGIS" experiment assimilates in situ, OCO-2 land data, and OCO-2 ocean glint retrievals.

In situ CO_2 measurements are obtained from version 8.0 of the NOAA GLOBALVIEW plus Obspack dataset (Schuldt et al., 2022). These data are provided on the X2019 CO_2 scale but were back corrected to the X2007 CO_2 scale following Hall et al. (2021). We apply several filters to the in situ data before assimilation. Surface in situ CO_2 measurements are assimilated at their respective height above the surface, with inclusion criteria that the model surface elevation should differ by less than 500 m from the 15 arc-second ETOPO1 global elevation dataset (NOAA, 2021). Secondly, we only assimilate data with the CT_assim flag greater than or equal to one, which indicates data that is deemed assimilable for the NOAA CarbonTracker system. Finally, only measurements obtained between 11:00 and 17:00 local time are assimilated (when the atmospheric boundary layer is well mixed). The sites assimilated are: amt, bck, bmw, bra, brw, cba, cby, chl, cps, crv, egb, esp, est, etl, fsd, inu, inx, key, kum, lef, lew, llb, sct, sgp, uta, wbi, wgc, wkt, wsa. The sites with CT_assim$\geq$ 1 that are not assimilated are: mbo, mex, mlo, mwo, nwr, omp, uts, wsd. We note that some sites with CT_assim= 0 may be assimilable, but more work is needed to characterize their suitability for assimilation. We apply the CT_MDM "model-data-mismatch" values as uncertainties on assimilated measurements. All aircraft data, including the ACT-America campaign data (Davis et al., 2021, 2018; Wei et al., 2021), are withheld for validation purposes. Monthly maps of data density are shown in Figure S1.

We employ X_{CO_2} retrieved using version 10 of NASA's Atmospheric CO_2 Observations from Space (ACOS) full-physics retrieval algorithm (O'Dell et al., 2018). Subsequently, OCO-2 "buddy" super-observations are calculated by averaging individual soundings into super-observations at a spatial resolution of 0.5° × 0.5° within the same orbit, assigning equal weights, following the approach by Liu et al. (2017). Monthly maps illustrating data density are shown in Figure S2.

The global inversions discussed in Sec. 3.2.2 follow an identical set-up as the nested inversions, with the same flux datasets regrided to 4° × 5° globally.

2.1.2 Observing System Simulation Experiments

A series of OSSEs are conducted to explore the impact of observational coverage in quantifying carbon cycle perturbations resulting from extreme events. These OSSEs cover the same two year period as the real data inversions. Four OSSE experiments are carried out: IS, LNLG, LNLGOGIS, and one for a new hypothetical space-based observing system that provides daily X_{CO_2} retrievals at 13:00 (1 pm). This hypothetical system, referred to as the ideal LEO mission, could comprise a dense constellation of low Earth orbit (LEO) sensors. The OSSEs are carried out following the same setup as the real data experiments, while the true atmospheric CO_2 boundary and initial conditions are implemented for the nested inversion.

For the ideal LEO mission, pseudo-observations are generated as follows: 1 pm observations within each land $0.5° \times 0.625°$ grid cell are filtered to exclude instances of low-light conditions, cloudy conditions, and when the surface is covered by snow or ice. Fractional snow cover and cloud cover data are obtained from the MERRA-2 reanalysis dataset (Gelaro et al., 2017). Measurements are excluded for grid cells with a fractional area of land snow cover (FRSNO) greater than 75% and total cloud area fraction (ISCCPCLDFRC) greater than 75% from the International Satellite Cloud Climatology Project (ISCCP). Additionally, observations with an atmospheric path exceeding six air-masses are removed. We allow one super-obs within each gridcell per day. The uncertainty on the super-obs is defined to be 0.7 ppm, roughly matching OCO-2. Monthly maps of data density for the ideal LEO mission are shown in Fig. S3.

True NEE fluxes for the OSSEs are generated by combining a climatological NEE seasonal cycle with anomalies from the bottom-up datasets. Climatological true NEE fluxes are obtained from the CASA-GFED3 model, which undergoes downscaling from monthly to three-hourly fluxes. These fluxes align with those described in Appendix 3 of Byrne et al. (2020). Interannual variations in the true fluxes are introduced by incorporating NEE anomalies taken to be 65% of the mean bottom-up GPP anomalies across the five datasets (see Sec. 2.2). Pseudo-observations are then generated by conducting a forward simulation using the nested model.

2.2 Remote-sensing bottom-up ΔGPP and ΔNEE estimates

We generate an ensemble of five bottom-up ΔGPP estimates by combining a number of remote-sensing-based GPP datasets. Four of these are obtained from existing datasets: 8 day FLUXCOM remote-sensing-based (RS) GPP (Jung et al., 2020), FluxSat Version 2 (Joiner & Yoshida, 2020), GOSIF GPP (Li & Xiao, 2019), and the $\mathrm{NIR_V}$-based GPP estimates of L. He et al. (2022). All of these data are regridded from their native resolution to weekly temporal resolution and $0.5° \times 0.625°$ spatial resolution.

In addition, we estimate GPP directly from TROPOMI SIF data. This followed the same approach as Yin et al. (2020). Two GPP estimates are then calculated using land-cover-dependent SIF-to-GPP scaling factors from Li et al. (2018) and Y. Sun et al. (2017), which were adjusted by a factor of 0.64 to account for difference retrieval wavelegnths between OCO-2 and TROPOMI (740 nm vs 757 nm). These factors were then applied to gridded SIF data (0.08333° spatial and 8 day temporal resolution), while accounting for the fractional vegetation cover within each gridcell. The GPP estimates were then regridded to $0.5° \times 0.625°$ spatial resolution. Any data gaps within the growing season are then filled by linear interpolation over time, while GPP is assumed to be zero for data gaps outside the growing season. Finally the two GPP estimates are averaged.

From these GPP datasets, we estimate an anomaly in NEE between 2018 and 2019 by assuming the NEE anomaly is equal to the NPP anomaly, which is itself related to the GPP anomaly by:

$$\Delta\mathrm{NEE} = -\Delta\mathrm{NPP} = -0.60 \times \Delta\mathrm{GPP} \tag{1}$$

The factor of 0.60 is an estimate of the carbon use efficiency (CUE), and is a relatively high estimate (Manzoni et al., 2018; Y. He et al., 2018), though may be representative of corn (S. Yu et al., 2023; Campioli et al., 2015). We assume an error of ± 0.1 in CUE, and perform error analysis using factors of 0.5 and 0.7. The conversion of ΔNPP to ΔNEE assumes that ΔHR is negligible. This is likely a poor assumption, but a limitation of remote-sensing estimates that are insensitive to HR variations. Previously, Yin et al. (2020) showed that bottom-up ΔNEE estimated assuming negligible ΔHR could reasonably reproduce observed atmospheric CO_2 enhancements during the 2019 US Midwest floods, providing some evidence that ΔHR variations have a secondary impact.

2.3 State crop yields and NPP

Crop yields, which represents the amount of crop biomass removed from the field during harvest events, have been estimated using county-level crop yield data from the US Department of Agriculture (USDA) - National Agricultural Statistics Service (NASS) (USDA-NASS, 2020). The carbon content of crop yields was derived from the relationship:

$$\mathrm{Y_C} = \mathrm{Y_{NASS}} \times \mathrm{DM} \times \mathrm{C_f}, \tag{2}$$

where $\mathrm{Y_C}$ is the crop yield, in units of carbon, $\mathrm{Y_{NASS}}$ is the annual county-level crop yield data from USDA-NASS, DM is the dry matter content for each crop, and $\mathrm{C_f}$ is carbon content crop factor. Crop NPP ($\mathrm{NPP_{crop}}$), representing the net carbon uptake by crops, was derived from the crop yield estimates using the following equation:

$$\mathrm{NPP_{crop}} = \mathrm{Y_{NASS}} \times \frac{1}{\mathrm{HI}} \times (1 + \mathrm{R_{RS}}) \times \mathrm{DM} \times \mathrm{C_f}, \tag{3}$$

where HI is the harvest index for each crop, i.e., the proportion of harvested material (e.g., grains) in relation to total crop aboveground biomass; and RRS is the root:shoot ratio for each crop. We used crop-specific factors for dry matter, root:shoot ratios, harvest indices, and carbon content following the methods in West et al. (2010, 2011) and Ogle et al. (2015). Crop yields and NPP were estimated for over 20 crops, which together represented >99% of total US crop production (USDA-NASS, 2020). Uncertainty in estimates were propagated through a Monte Carlo approach with 10,000 replicates and probability distribution functions for all input data and factors. The results are based on the mean and 95% confidence intervals from the final distribution of simulated values. We note that NASS only included uncertainty in crop yield data for 2020 so we assumed a similar level of uncertainty in crop yields for the other years.

3 Results

3.1 Flood-induced NEE anomalies

Figure 1a–b illustrates the difference in June-July NEE between 2019 and 2018 ($\Delta\mathrm{NEE} = \mathrm{NEE_{2019}} - \mathrm{NEE_{2018}}$) for both the remote-sensing bottom-up (ensemble mean) and top-down (LNLGOGIS) estimates. The analyses reveal a significant decrease in CO_2 uptake (positive ΔNEE) specifically in the US Midwest region. This pronounced positive ΔNEE signal in the US Midwest stands out compared to the rest of the continent. Figure 1c presents the 5 week running mean time series of ΔNEE over the US Midwest. Both the top-down and bottom-up estimates depict a positive ΔNEE signal throughout Jun–Jul, with the anomaly peaking towards the end of June. However, during Aug-Sep, the top-down and bottom-up estimates suggest a negative ΔNEE in the US Midwest. Across the rest of the continent (Figure 1d), anomalies are weaker. The top-down estimate suggests a positive anomaly outside the US Midwest during August, while the bottom-up estimate suggests no significant anomalies. The supplementary materials display the maps and timeseries for the other top-down experiments (Fig. S4) and individual bottom-up datasets (Fig. S5).

Figure 2 shows US Midwest ΔNEE for each of the top-down and bottom-up estimates. In addition, an estimate of the anomaly in net primary production for crops ($\Delta\mathrm{NPP_{crop}}$) derived from crop yield data is shown. All estimates suggest positive ΔNEE over the study period (-6–85 TgC for top-down, 15–78 TgC for bottom-up, and 36–65 TgC for yield-based estimates). We find that June-July ΔNEE drives the annual anomaly with uptake reduced by 24–76 TgC in top-down estimates and 38–131 TgC in bottom-up estimates. The bottom-up estimates suggest this is moderated when integrating across the growing season due to greater carbon uptake during Aug-Sep (-56 TgC to -15 TgC), while the top-down estimates are less consistent during Aug-Sep, ranging from -37 TgC to 34 TgC. Figure S6 demonstrates that the bottom-up and top-down ΔNEE generally show similar June-July ΔNEE across the CONUS Climate Assessment Regions. In particular, we

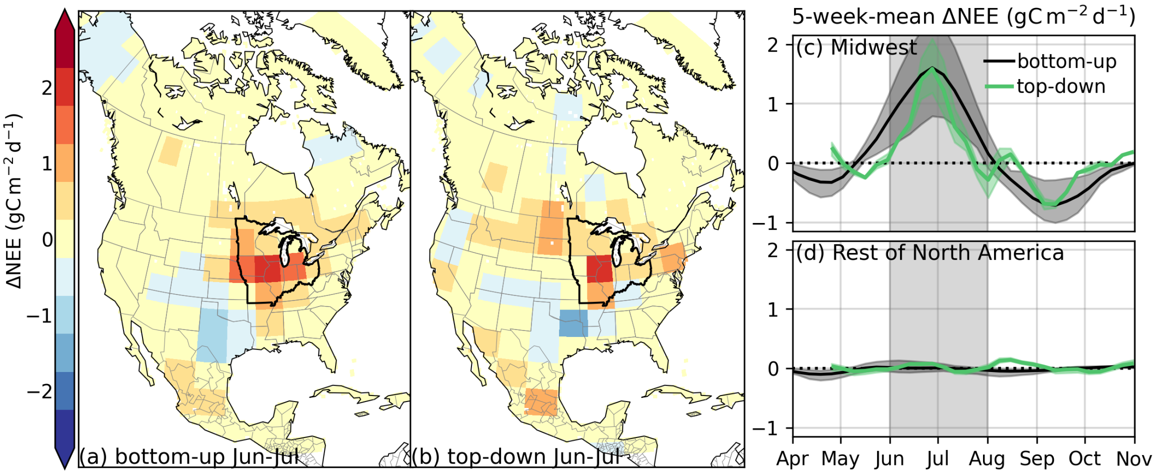

Figure 1. (a) Bottom-up and (b) top-down (LNLGOGIS) spatial patterns of June–July mean ΔNEE ($NEE_{2019} - NEE_{2018}$) at 4° × 5° spatial resolution. (c) US Midwest and (d) rest of North America 5-week-mean ΔNEE. The US Midwest is defined as the area within Illinois, Indiana, Iowa, Michigan, Minnesota, Missouri, Ohio, and Wisconsin and is indicated by the black outline in panels (a) and (b). The shading shows the range around the mean estimate for the inversions using three different priors and for the five bottom-up GPP datasets.

find that all estimates obtain negative ΔNEE across the Southern Great Plains (-22 to -46 TgC), resulting from the 2018 drought (Turner et al., 2021).

These findings suggest that both in situ and OCO-2 data provide adequate observational coverage to detect the June-July ΔNEE signal resulting from the 2019 US Midwest floods. However, some differences are also evident. The experiments disagree in the sign of Aug-Sep ΔNEE. The IS experiment shows negative Aug-Sep ΔNEE that largely compensates for the positive June–July ΔNEE. Conversely, the LNLG experiment gives positive Aug–Sep ΔNEE but the smallest June–July ΔNEE. There are some spatial differences as-well, for example, the IS experiment suggests larger positive ΔNEE in western Canada and negative ΔNEE in the southeast during Jun-Jul than the other experiments (Fig. S4). The LNLGIS and LNLGOGIS experiments yield quite similar results. The relative accuracy of these different estimates is challenging to evaluate, as a number of different drivers could contribute to differences but all experiments exhibit good agreement with independent aircraft CO_2 measurements during 2018 and 2019 (Text S1, Fig. S7-S12). The disparities between experiments may arise from differences in observational coverage and this hypothesis is examined in Sec. 3.2.1.

The bottom-up estimates show some notable differences in the magnitude of ΔNEE over the US Midwest and the spatial structure of ΔNEE outside the US Midwest (Fig. S5). FLUXCOM consistently displays the weakest ΔNEE signal, and has been previously shown to underestimate interannual variations in NEE and GPP (Jung et al., 2020). Outside the US Midwest, the NIR_V-based estimate shows negative values across the western half of North America, which are not observed in any other estimates, while the TROPOMI-based estimate indicates positive ΔNEE across a large portion of eastern Canada. Consequently, the net June–July ΔNEE signal outside the US Midwest varies across datasets, ranging from -218 TgC to 187 TgC.

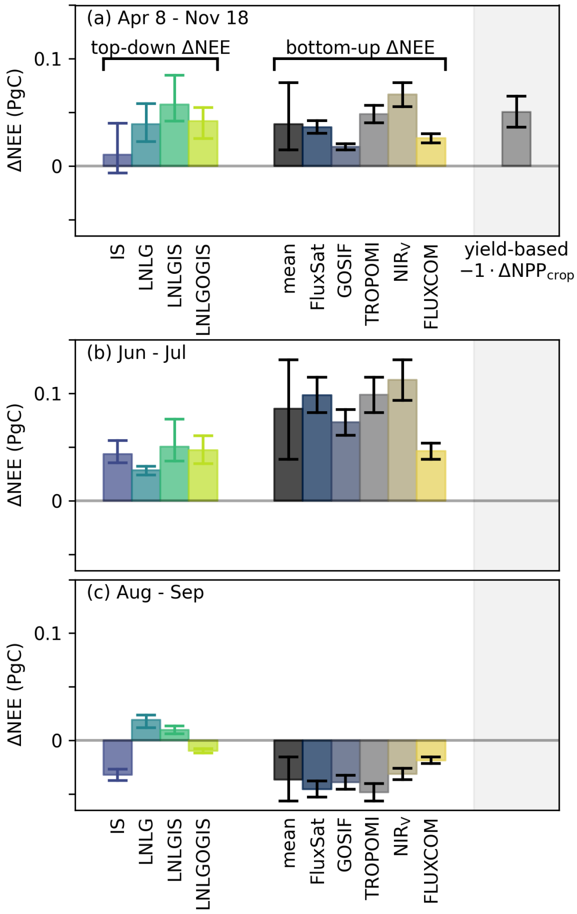

Figure 2. Top-down ΔNEE, bottom-up ΔNEE, and yield-based ΔNPP for crops (ΔNPP_{crop}) over the US Midwest. ΔNEE is calculated for (a) the entire inversion period (April 8th – Nov 18th), (b) June-July and (c) Aug-Sep. The top-down estimates show the mean and range obtained using three different priors. Uncertainty bars for the top-down estimates show the range using three priors, while the uncertainties on the bottom-up show the range of using carbon use efficiencies of 0.5–0.7.

3.2 Sensitivity experiments

3.2.1 Impact of observational coverage

Although both the in situ network and OCO-2 were able to identify a positive US Midwest ΔNEE signal, we found substantial differences between the top-down experiments. Here we perform OSSEs to investigate whether gaps in observational coverage could explain these differences. Further, we test whether increased observational coverage (in an ideal LEO constellation) would substantially improve top-down estimates of extreme-event-driven carbon cycle perturbations.

Figure 3 shows the true and posterior ΔNEE for the OSSEs. All OSSEs recover positive ΔNEE to the US Midwest, consistent with the real data experiments. However, June-July US Midwest ΔNEE is underestimated by 43% for IS, 75% for LNLG, 48% for LNLGOGIS and 15% for the ideal LEO constellation. In addition, the inversions tend to introduce a positive June–July ΔNEE outside the US Midwest that is not present in the truth. Over June-July, the true continental-scale ΔNEE is 89 TgC, while the mean inversion estimates are 163 TgC (error of +74 TgC) for IS, 93 TgC (error of +4 TgC) for LNLG, 68 TgC (error of -21 TgC) for LNLGOGIS, and 93 TgC (error of +4 TgC) for ideal LEO. A similar large continental-scale positive June–July ΔNEE was found for the real data IS experiment (Fig. S4ci). One possible explanation is that the limited spatial coverage of the in situ (Fig. S1) data may limit the ability to capture aggregate continental-scale budgets using a one-way nested system.

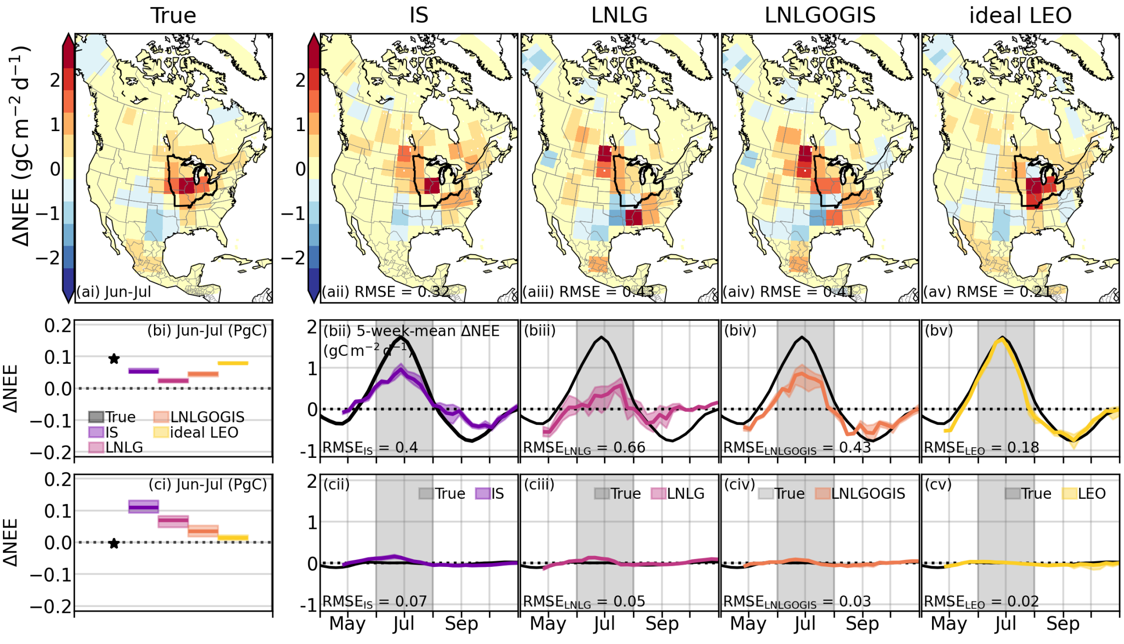

Figure 3. ΔNEE estimates for the OSSEs. Panel (ai) shows the true June-July ΔNEE maps, while panels (aii)–(av) show the OSSE posterior June-July ΔNEE maps and RMSE across grid-cells (gC m^{-2} d^{-1}). The net US Midwest Jun-Jul ΔNEE (PgC) is shown for each OSSE in panel (bi), and the timeseries of 5-week-mean ΔNEE is shown for each experiment in panels (bii)–(bv), with RMSE across weeks (gC m^{-2} d^{-1}). The same quantities are show for the rest of North America in panels (ci)–(cv).

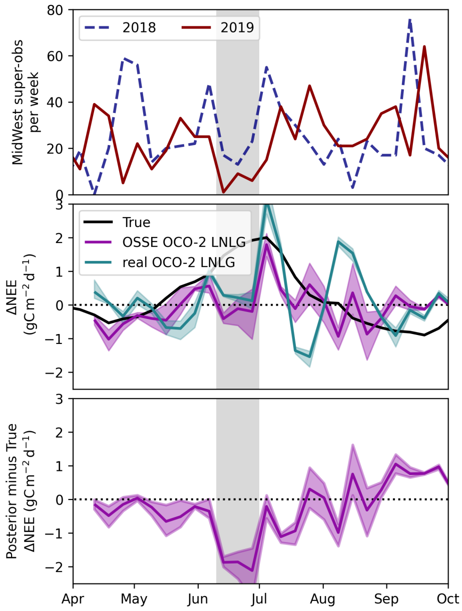

Figure 4. Weekly timeseries of (top) number of OCO-2 super-obs in the US Midwest for 2018 and 2019. (middle) Weekly ΔNEE in the US Midwest for the truth, OCO-2 OSSE and real OCO-2 LNLG experiment. (bottom) Difference between posterior and true ΔNEE for the OCO-2 OSSE. The shading shows the range around the mean estimate for the inversions using three different priors.

Overall, the LNLG OSSE shows the worst performance at isolating the US Midwest ΔNEE. We suggest that this could be related to interannual variations in the observational coverage. Figure 4a shows that the number of LNLG weekly samplings over the US Midwest can be quite variable from year to year. In particular, there are only 16 super-obs in the US Midwest during the three week period of June 11, 2019 to July 2 2019. This coincides with near zero ΔNEE for both the real data LNLG inversion and OSSE (Fig. 4b), and the period with the largest error in ΔNEE for the OSSE (Fig. 4c). These results suggest that data gaps in OCO-2, particularly differences in observational coverage between years, limit our ability to estimate inter-annual variations in NEE at high spatio-temporal resolution.

The increased sampling from combining the datasets (LNLGOGIS) appears to moderately improve performance, particularly in isolating June–July ΔNEE to the US Midwest (relative to LNLG) and better capturing the continental-scale ΔNEE (relative to IS). However, the ideal LEO constellation results in much improved performance in both space and time. The ideal LEO constellation reduces June-July RMSE across $4° \times 5°$ regions by 34–51% and the 5-week-mean ΔNEE US Midwest RMSE by 55–73%. This comparison suggests that top-down estimates of extreme-event-driven perturbations to carbon uptake remain observationally-limited and that expanded space-based observing systems will improve these estimates.

3.2.2 Comparison between nested and global inversions

The nested CMS-Flux inversion system in this study offers both advantages and disadvantages compared to a global CMS-Flux inversion system. One major advantage is the ability to run transport at a higher resolution ($0.5° \times 0.625°$) compared to the global

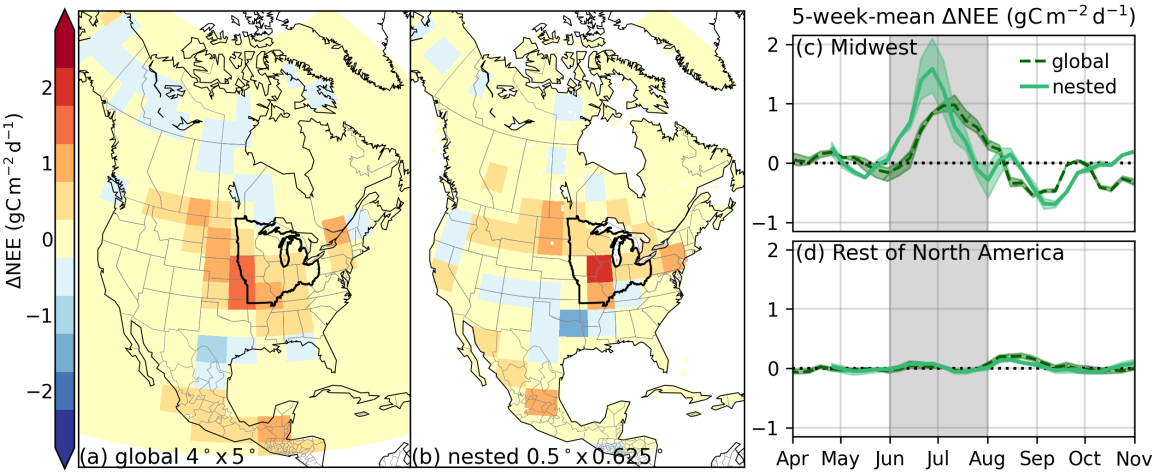

Figure 5. Comparison of the global 4° × 5° and nested inversion results. Maps of June–July ΔNEE from the LNLGOGIS experiment are shown for (a) the global 4° × 5° inversion and (b) the nested inversion. Weekly ΔNEE in the US Midwest after applying a 5-week running mean are also show for (c) the US Midwest and (d) rest of North America.

system (4°×5°). This higher resolution enables tracer transport to be closer to the parent model, as spatial averaging of meteorological fields can average out eddy transport, particularly affecting vertical motions (Stanevich et al., 2020). Additionally, a higher resolution model grid reduces representativeness errors, allowing better representation of fine-scale features that influence observations, such as topography. The primary disadvantage of the one-way nested system used in this study is the assumption of perfect boundary conditions and the inability to assimilate atmospheric CO_2 observations outside the nested domain. In a global inversion, fluxes over North America would impact measurements downwind, providing a powerful constraint on large-scale fluxes, including the net North American flux (Liu et al., 2015). A bias in flux at the continental scale would affect CO_2 fields across the entire Northern Hemisphere. Since the nested inversion lacks this constraint, significant errors in continental-scale fluxes may go undetected. Furthermore, biases in the imposed boundary CO_2 fields can propagate into optimized fluxes.

In order to assess the performance of the one-way nested inversion, we compare the obtained ΔNEE with the global version of CMS-Flux using the same inversion configuration, whenever possible. Figure 5 presents the results for both the global and nested versions of CMS-Flux. It is observed that the nested version of CMS-Flux effectively isolates ΔNEE to the US Midwest region during June–July. In contrast, the global model exhibits spatially broader positive ΔNEE across the US Midwest and Great Plains, resulting in a significantly reduced ΔNEE estimate for the US Midwest during June–July. The spatial pattern of ΔNEE for the nested model aligns more closely with the bottom-up estimate, suggesting that this system better captures the overall event. This indicates that, considering the observational coverage provided by LNLGOGIS, the benefits of reduced transport and representativeness errors in the nested model outweigh the detrimental impact of a limited domain.

We note that achieving good performance with nested version of CMS-Flux was challenging, and required a number of trial-and-error inversions. This included varying the size of the state vector spatially (0.5°×0.625° versus 4°×5° grid) and temporally (weekly, bi-weekly, monthly intervals). It also involved adjusting the prior constraints (optimizing HR rather than NEE, adjusting prior uncertainties). We suggest that these challenges are due to greater regularization requirements for the nested model in comparison to the global model. The sensitivities of observations to surface fluxes are limited to 1–2 weeks by the one-way nesting, such that large-scale constraints are imposed by the boundary conditions (Feng, Lauvaux, Davis, et al., 2019; Feng, Lauvaux, Keller, et al., 2019). Thus, the flux signal in the domain is generally much smaller than for the global model, where downwind observations provide important information for upwind continental-scale regions (Liu et al., 2015). We suggest that imposing an error correlation length between state-vector elements may be an effective approach for regularization in a nested inversion context (see Sec. 4.1), however, this is beyond the scope of our current study.

4 Discussion and Conclusions

Both top-down and bottom-up approaches capture a flood-induced reduction in net carbon uptake during the 2019 US Midwest floods. The top-down approach gave mean estimates of 11 TgC (IS), 39 TgC (LNLG), 57 TgC (LNLGIS), 42 TgC (LNLGOGIS) for US Midwest growing season ΔNEE. Meanwhile, the bottom-up datasets gave a mean estimate of 39 TgC (range: 15–78 TgC). These magnitudes are significant compared to anthropogenic emissions, amounting to as much as 28% of the US Midwest's annual fossil fuel emissions (300 $\mathrm{TgC\,yr^{-1}}$ for 2019, U.S. Energy Information Administration (2023)). In addition, this anomaly is comparable to the year-to-year variations in fossil fuel emissions (SD: 25 $\mathrm{TgC\,yr^{-1}}$), even including the reduction of regional emissions by 36 $\mathrm{TgC\,yr^{-1}}$ due to COVID-19 lockdowns in 2020.

In the context of more frequent heat and precipitation extremes (Seneviratne et al., 2021), accurate estimates of the carbon cycle responses will be critical for monitoring carbon budgets and evaluating carbon-climate feedbacks. The results of this study show that both top-down and bottom-up approaches demonstrate skill in capturing ΔNEE resulting from the 2019 Midwest floods, however a number of deficiencies were also identified. In the following sub-sections, we highlight current challenges and opportunities in quantifying carbon cycle extremes.

4.1 Top-down

Observational gaps in atmospheric CO_2 observations are identified as a key limitation in applying top-down methods to quantify extreme-event-driven ΔNEE, consistent with recent studies of the European carbon budget (W. He et al., 2023; Munassar et al., 2022; Monteil et al., 2020; Thompson et al., 2020). Through a series of OSSE experiments, it was demonstrated that gaps in both the in situ network and OCO-2 sampling impact the accuracy of ΔNEE estimates. While assimilating these two datasets concurrently partially mitigates the issue, fully resolving the problem requires expanded observations. Coverage similar to the ideal LEO observing system could be developed by combining multiple individual satellites, and motivates future studies that assimilate X_{CO_2} retrievals from multiple space-based observing systems concurrently (e.g., GOSAT, OCO-2, and OCO-3). In addition, efforts should be made to ensure consistency in X_{CO_2} retrievals between existing and planned missions (e.g., CO2M, GOSAT-GW). Expanding the in situ network would also likely enhance the ability to capture regional flux anomalies more effectively, however, this was not specifically explored.

Although current observing gaps are found to be a major limitation, there may be approaches to better regularize the inverse problem and reduce the impact of these gaps. In particular, applying off-diagonal co-variances in the prior error covariance matrix could be employed to adjust fluxes where observations are missing (Chen et al., 2023). Applying spatial co-variances will likely be especially important for in situ inversions, while applying temporal co-variances may be most useful for OCO-2 X_{CO_2} inversions. Of course, such an approach will only improve flux estimates if spatial and temporal co-variances are truly present, such that this approach will be limited by a correlation length scale. In addition, imposing realistic prior IAV could also be a fruitful approach, as has been done in previous studies evaluating the 2019 US Midwest floods (Yin et al., 2020; Balashov et al., 2022). However, high-confidence is needed in imposed prior IAV, as inaccurate prior IAV can significantly degrade posterior IAV estimates (Byrne et al., 2019). Text S2 and Figs. S13-15 show that imposing bottom-up IAV in the prior results in larger posterior ΔNEE anomalies during the Midwest Floods for all experiments. This is consistent with the ΔNEE anomalies being underestimated when using climatological priors, as was found in the OSSEs.

Finally, this study investigated the utility of a one-way nested version of CMS-Flux with $0.5° \times 0.625°$ spatial resolution relative to the global model at $4° \times 5°$ degree spatial resolution. We note that developing a nested inversion system involved considerable effort in tuning the state vector structure, assimilation window, and prior constraints. Nevertheless, we found that the nested model better allocated flood-induced ΔNEE to the US Midwest, suggesting that the improved model transport and observation representation of the nested model improved the overall performance relative to the global model, consistent with several recent studies (Monteil et al., 2020; Hu et al., 2019). However, the nested model has some disadvantages, especially the inability to assimilate downwind observations outside the model domain that may limit the utility of the nested model in other applications. Transport uncertainty and boundary condition errors may lead to significant challenges for nested inversions (Munassar et al., 2023; Kim et al., 2021; Chen et al., 2019; Lauvaux et al., 2012), but were not obvious in our analyses. We note that high-resolution models will be needed to take advantage of upcoming wide-swath sampling missions, such as CO2M (∼250 km swath) or GOSAT-GW (∼400 km swath).

4.2 Bottom-up

Remote-sensing-based bottom-up estimates of ΔNEE provided a consistent picture of reduced net uptake during the 2019 Midwest floods but differed significantly in magnitude. The primary source of this variability stems from translating space-based reflectance or SIF observations to GPP, leading to a range in ΔGPP between datasets of 120% of the mean. Indeed, estimating the magnitude of GPP from remote sensing datasets is challenging due to satellite signals that could be influenced by factors such as cloud coverage and soil background, in addition to calibration that is predominantly relying on benchmarks provided by eddy covariance sites. We encourage research into approaches that can reduce uncertainties on large-scale GPP magnitudes, possibly through top-down constraints from Carbonyl Sulphide.

Additional uncertainties were introduced in estimating ΔNEE from ΔGPP. Due to the inherent limitations of remote sensing, which can track GPP but not the total ecosystem respiration (the sum of HR and AR), certain assumptions must be made. First, to estimate AR, we assumed that ΔGPP and ΔNPP can be related through a constant carbon use efficiency (CUE) parameter that varies across vegetation type, age, and management practices (Campioli et al., 2015; DeLucia et al., 2007; Manzoni et al., 2018; Y. He et al., 2018; S. Yu et al., 2023). In our analysis, we adopted a mean value of 0.60 with an uncertainty of range 20% (0.5–0.7), which encompasses most literature estimates. Second, we assumed that the influence of ΔHR on the ΔNEE was negligible. The secondary impact of ΔHR is supported by Yin et al. (2020), who were able to reasonably reproduce observed atmospheric CO_2 enhancements during the 2019 US Midwest floods while neglecting ΔHR variations. Still, it is important to note that HR is sensitive to variations in temperature and moisture. Terrestrial biosphere models could serve as potential tools for estimating ΔHR (e.g., Balashov et al. (2022)) as remote sensing does not adequately capture variations in HR, which is significantly influenced by the availability of labile carbon. However, the accuracy of these model-driven estimates remains challenging to verify.

5 Open Research

Once accepted for publication, the prior and posterior fluxes, TROPOMI-based GPP, and NIR_V-based GPP will be archived with a DOI. During the review processes the data are available by contacting Brendan Byrne. The atmospheric CO_2 inversion analyses performed in this study used the CMS-Flux model, which is based on the GEOS-Chem Adjoint model that can be accessed from the GEOS-Chem Wiki (https://wiki.seas.harvard.edu/geos-chem). OCO-2 X_{CO_2} Lite files can be downloaded from the GES DISC (https://disc.gsfc.nasa.gov). In Situ CO_2 measurements (Schuldt et al., 2022) can be downloaded from https://gml.noaa.gov/ccgg/obspack/. GFED biomass burning emissions (van der Werf et al., 2017) were downloaded from https://globalfiredata.org/. Fossil fuel emissions (Basu & Nassar, 2021) were downloaded from https://doi.org/10.5281/zenodo.4776925. MERRA-2 reanalysis data (Gelaro et al., 2017) was downloaded from https://disc.gsfc.nasa.gov/. TROPOMI SIF data are accessed online at https://data.caltech.edu/records/1347 (DOI: 10.22002/D1.1347). FluxSat Version 2 (Joiner & Yoshida, 2021) were downloaded from the ORNL DAAC (https://daac.ornl.gov). GOSIF GPP (Li & Xiao, 2019) were downloaded from http://data.globalecology.unh.edu/. FLUXCOM GPP (Jung et al., 2020) was downloaded from the aata portal of the Max Planck Institute for Biogeochemistry (https://www.bgc-jena.mpg.de/geodb/projects/Home.php).

Acknowledgments

The research carried out at the Jet Propulsion Laboratory, California Institute of Technology, was under a contract with the National Aeronautics and Space Administration. Funding for the research was from the NASA CMS (grant nos. 80NSSC21K1060, 80NM0018F0583) and OCO science team (grant np. 80NM0018F0583) programs. Resources supporting this work were provided by the NASA High-End Computing (HEC) program through the NASA Advanced Supercomputing (NAS) Division at Ames Research Center.

References

Balashov, N., Ott, L. E., Weir, B., Basu, S., Davis, K. J., Miles, N. L., ... Stauffer, R. M. (2022). Flood impacts on net ecosystem exchange in the midwestern and southern united states in 2019. doi: 10.1002/essoar.10512359.1

Barkhordarian, A., Bowman, K. W., Cressie, N., Jewell, J., & Liu, J. (2021). Emergent constraints on tropical atmospheric aridity—carbon feedbacks and the future of carbon sequestration. *Environmental Research Letters*, *16*(11), 114008.

Basu, S., & Nassar, R. (2021, January). *Fossil Fuel CO Emissions for the OCO2 Model Intercomparison Project (MIP).* Zenodo. Retrieved from `https://doi.org/10.5281/zenodo.4776925` (Previous versions available from (2018): https://g mao.gsfc.nasa.gov/gmaoftp/sourish/ODIAC/2018/distr ib/, (2017): ftp://aftp.cmdl.noaa.gov/data/ccgg/OD IAC/2017/distrib/, (2016): ftp://aftp.cmdl.noaa.go v/data/ccgg/ODIAC/2016/distrib/, (2015a): ftp://af tp.cmdl.noaa.gov/data/ccgg/ODIAC/2015a/distrib/) doi: 10.5281/zenodo.4776925

Byrne, B., Baker, D. F., Basu, S., Bertolacci, M., Bowman, K. W., Carroll, D., ... Zeng, N. (2023). National CO_2 budgets (2015–2020) inferred from atmospheric CO_2 observations in support of the global stocktake. *Earth System Science Data*, *15*(2), 963–1004. Retrieved from `https://essd.copernicus.org/articles/15/963/2023/` doi: 10.5194/essd-15-963-2023

Byrne, B., Jones, D. B. A., Strong, K., Polavarapu, S. M., Harper, A. B., Baker, D. F., & Maksyutov, S. (2019). On what scales can gosat flux inversions constrain anomalies in terrestrial ecosystems? *Atmos. Chem. Phys.*, *19*(20), 13017–13035. Retrieved from `https://www.atmos-chem-phys.net/19/13017/2019/` doi: 10.5194/acp-19-13017-2019

Byrne, B., Liu, J., Lee, M., Baker, I. T., Bowman, K. W., Deutscher, N. M., ... Wunch, D. (2020). Improved constraints on northern extratropical CO_2 fluxes obtained by combining surface-based and space-based atmospheric CO_2 measurements. *Journal ofGeophysical Research: Atmospheres*, *125*. doi: 10.1029/2019JD032029

Byrne, B., Liu, J., Lee, M., Yin, Y., Bowman, K. W., Miyazaki, K., ... Paton-Walsh, C. (2021). The carbon cycle of southeast Australia during 2019–2020: Drought, fires, and subsequent recovery. *AGU Advances*, *2*(4), e2021AV000469. doi: 10.1029/2021AV000469

Campioli, M., Vicca, S., Luyssaert, S., Bilcke, J., Ceschia, E., Chapin III, F. S., ... others (2015). Biomass production efficiency controlled by management in temperate and boreal ecosystems. *Nature geoscience*, *8*(11), 843–846.

Chen, H. W., Zhang, F., Lauvaux, T., Davis, K. J., Feng, S., Butler, M. P., & Alley, R. B. (2019). Characterization of regional-scale co2 transport uncertainties in an ensemble with flow-dependent transport errors. *Geophysical Research Letters*, *46*(7), 4049–4058.

Chen, H. W., Zhang, F., Lauvaux, T., Scholze, M., Davis, K. J., & Alley, R. B. (2023). Regional co_2 inversion through ensemble-based simultaneous state and parameter estimation: TRACE framework and controlled experiments. *Journal of Advances in Modeling Earth Systems*, *15*(3), e2022MS003208.

Ciais, P., Reichstein, M., Viovy, N., Granier, A., Ogée, J., Allard, V., ... others (2005). Europe-wide reduction in primary productivity caused by the heat and drought in 2003. *Nature*, *437*(7058), 529–533. doi: https://doi.org/10.1038/nature03972

Davis, K. J., Browell, E. V., Feng, S., Lauvaux, T., Obland, M. D., Pal, S., ... others (2021). The atmospheric carbon and transport (act)-america mission. *Bulletin of the American Meteorological Society*, *102*(9), E1714–E1734.

Davis, K. J., Obland, M., Lin, B., Lauvaux, T., O'Dell, C., Meadows, B., ... Pauly, R. (2018). *ACT-America: L3 merged in situ atmospheric trace gases and flask data, eastern usa.* ORNL Distributed Active Archive Center. Retrieved from `https://daac.ornl.gov/cgi-bin/dsviewer.pl?ds_id=1593` doi: 10.3334/ORNLDAAC/1593

DeLucia, E., Drake, J. E., Thomas, R. B., & Gonzalez-Meler, M. (2007). Forest carbon use efficiency: is respiration a constant fraction of gross primary production? *Glob. Change Biol.*, *13*(6), 1157–1167.

Fargione, J. E., Bassett, S., Boucher, T., Bridgham, S. D., Conant, R. T., Cook-Patton, S. C., ... others (2018). Natural climate solutions for the United States. *Science Advances*, *4*(11), eaat1869.

Feldman, A. F., Zhang, Z., Yoshida, Y., Chatterjee, A., & Poulter, B. (2023). Using Orbiting Carbon Observatory-2 (OCO-2) column CO_2 retrievals to rapidly detect and estimate biospheric surface carbon flux anomalies. *Atmospheric Chemistry and Physics*, *23*(2), 1545–1563. Retrieved from `https://acp.copernicus.org/articles/23/1545/2023/` doi: 10.5194/acp-23-1545-2023

Feng, S., Lauvaux, T., Davis, K. J., Keller, K., Zhou, Y., Williams, C., ... Baker, I. (2019). Seasonal characteristics of model uncertainties from biogenic fluxes, transport, and large-scale boundary inflow in atmospheric co_2 simulations over north america. *J. Geophys. Res.-Atmos.*, *124*(24), 14325–14346. doi: 10.1029/2019JD031165

Feng, S., Lauvaux, T., Keller, K., Davis, K. J., Rayner, P., Oda, T., & Gurney, K. R. (2019). A road map for improving the treatment of uncertainties in high-resolution regional carbon flux inverse estimates. *Geophysical Research Letters*, *46*(22), 13461–13469.

Gelaro, R., McCarty, W., Suárez, M. J., Todling, R., Molod, A., Takacs, L., ... others (2017). The modern-era retrospective analysis for research and applications, version 2 (MERRA-2). *J. Climate*, *30*(14), 5419–5454.

Hall, B. D., Crotwell, A. M., Kitzis, D. R., Mefford, T., Miller, B. R., Schibig, M. F., & Tans, P. P. (2021). Revision of the World Meteorological Organization Global Atmosphere Watch (WMO/GAW) CO_2 calibration scale. *Atmospheric Measurement Techniques*, *14*(4), 3015–3032. Retrieved from `https://amt.copernicus.org/articles/14/3015/2021/` doi: 10.5194/amt-14-3015-2021

He, L., Byrne, B., Yin, Y., Liu, J., & Frankenberg, C. (2022). Remote-sensing derived trends in gross primary production explain increases in the CO_2 seasonal cycle amplitude. *Global Biogeochemical Cycles*, *36*(9), e2021GB007220. doi: 10.1029/2021GB007220

He, W., Jiang, F., Ju, W., Byrne, B., Xiao, J., Nguyen, N. T., … others (2023). Do state-of-the-art atmospheric co2 inverse models capture drought impacts on the european land carbon uptake? *Journal of Advances in Modeling Earth Systems*, *15*(6), e2022MS003150.

He, Y., Piao, S., Li, X., Chen, A., & Qin, D. (2018). Global patterns of vegetation carbon use efficiency and their climate drivers deduced from MODIS satellite data and process-based models. *Agricultural and Forest Meteorology*, *256-257*, 150-158. Retrieved from `https://www.sciencedirect.com/science/article/pii/S0168192318300923` doi: https://doi.org/10.1016/j.agrformet.2018.03.009

Hu, L., Andrews, A. E., Thoning, K. W., Sweeney, C., Miller, J. B., Michalak, A. M., … van der Velde, I. R. (2019). Enhanced North American carbon uptake associated with El Niño. *Science advances*, *5*(6), eaaw0076. doi: 10.1126/sciadv.aaw0076

Joiner, J., & Yoshida, Y. (2020). Satellite-based reflectances capture large fraction of variability in global gross primary production (GPP) at weekly time scales. *Agricultural and Forest Meteorology*, *291*, 108092. Retrieved from `https://www.sciencedirect.com/science/article/pii/S0168192320301945` doi: https://doi.org/10.1016/j.agrformet.2020.108092

Joiner, J., & Yoshida, Y. (2021). *Global modis and fluxnet-derived daily gross primary production, v2.* ORNL DAAC, Oak Ridge, Tennessee, USA. doi: 10.3334/ORNLDAAC/1835

Jung, M., Schwalm, C., Migliavacca, M., Walther, S., Camps-Valls, G., Koirala, S., … Reichstein, M. (2020). Scaling carbon fluxes from eddy covariance sites to globe: synthesis and evaluation of the FLUXCOM approach. *Biogeosciences*, *17*(5), 1343–1365. Retrieved from `https://www.biogeosciences.net/17/1343/2020/` doi: 10.5194/bg-17-1343-2020

Kim, J., Polavarapu, S. M., Jones, D. B., Chan, D., & Neish, M. (2021). The resolvable scales of regional-scale co2 transport in the context of imperfect meteorology: The predictability of co2 in a limited-area model. *Journal of Geophysical Research: Atmospheres*, *126*(20), e2021JD034896.

Kirchmeier-Young, M. C., & Zhang, X. (2020). Human influence has intensified extreme precipitation in North America. *Proceedings of the National Academy of Sciences*, *117*(24), 13308-13313. Retrieved from `https://www.pnas.org/doi/abs/10.1073/pnas.1921628117` doi: 10.1073/pnas.1921628117

Lauvaux, T., Schuh, A. E., Uliasz, M., Richardson, S., Miles, N., Andrews, A. E., … Davis, K. J. (2012). Constraining the co_2 budget of the corn belt: exploring uncertainties from the assumptions in a mesoscale inverse system. *Atmospheric Chemistry and Physics*, *12*(1), 337–354. Retrieved from `https://acp.copernicus.org/articles/12/337/2012/` doi: 10.5194/acp-12-337-2012

Li, X., & Xiao, J. (2019). Mapping photosynthesis solely from solar-induced chlorophyll fluorescence: A global, fine-resolution dataset of gross primary production derived from OCO-2. *Remote Sensing*, *11*(21), 2563.

Li, X., Xiao, J., He, B., Altaf Arain, M., Beringer, J., Desai, A. R., ... others (2018). Solar-induced chlorophyll fluorescence is strongly correlated with terrestrial photosynthesis for a wide variety of biomes: First global analysis based on OCO-2 and flux tower observations. *Global change biology*, *24*(9), 3990–4008.

Liu, J., Bowman, K. W., & Henze, D. K. (2015). Source-receptor relationships of column-average CO_2 and implications for the impact of observations on flux inversions. *J. Geophys. Res.-Atmos.*, *120*(10), 5214–5236. doi: 10.1002/2014JD022914

Liu, J., Bowman, K. W., Schimel, D. S., Parazoo, N. C., Jiang, Z., Lee, M., ... Eldering, A. (2017). Contrasting carbon cycle responses of the tropical continents to the 2015–2016 El Niño. *Science*, *358*(6360). Retrieved from `http://science.sciencemag.org/content/358/6360/eaam5690` doi: 10.1126/science.aam5690

Manzoni, S., Čapek, P., Porada, P., Thurner, M., Winterdahl, M., Beer, C., ... Way, D. (2018). Reviews and syntheses: Carbon use efficiency from organisms to ecosystems – definitions, theories, and empirical evidence. *Biogeosciences*, *15*(19), 5929–5949. Retrieved from `https://bg.copernicus.org/articles/15/5929/2018/` doi: 10.5194/bg-15-5929-2018

Monteil, G., Broquet, G., Scholze, M., Lang, M., Karstens, U., Gerbig, C., ... Walton, E. M. (2020). The regional european atmospheric transport inversion comparison, eurocom: first results on european-wide terrestrial carbon fluxes for the period 2006–2015. *Atmospheric Chemistry and Physics*, *20*(20), 12063–12091. Retrieved from `https://acp.copernicus.org/articles/20/12063/2020/` doi: 10.5194/acp-20-12063-2020

Munassar, S., Monteil, G., Scholze, M., Karstens, U., Rödenbeck, C., Koch, F.-T., ... Gerbig, C. (2023). Why do inverse models disagree? a case study with two european co 2 inversions. *Atmospheric Chemistry and Physics*, *23*(4), 2813–2828.

Munassar, S., Rödenbeck, C., Koch, F.-T., Totsche, K. U., Gałkowski, M., Walther, S., & Gerbig, C. (2022). Net ecosystem exchange (nee) estimates 2006–2019 over europe from a pre-operational ensemble-inversion system. *Atmospheric Chemistry and Physics*, *22*(12), 7875–7892. Retrieved from `https://acp.copernicus.org/articles/22/7875/2022/` doi: 10.5194/acp-22-7875-2022

NOAA. (2021, July). *ETOPO 2022 15 Arc-Second Global Relief Model.* NOAA National Centers for Environmental Information. Retrieved from `https://doi.org/10.25921/fd45-gt74` doi: 10.25921/fd45-gt74

O'Dell, C. W., Eldering, A., Wennberg, P. O., Crisp, D., Gunson, M. R., Fisher, B., ... Velazco, V. A. (2018). Improved retrievals of carbon dioxide from orbiting carbon observatory-2 with the version 8 acos algorithm. *Atmos. Meas. Tech.*, *11*(12), 6539–6576. Retrieved from `https://www.atmos-meas-tech.net/11/6539/2018/` doi: 10.5194/amt-11-6539-2018

Ogle, S. M., Davis, K., Lauvaux, T., Schuh, A., Cooley, D., West, T. O., ... Denning, A. S. (2015, mar). An approach for verifying biogenic greenhouse gas emissions inventories with atmospheric CO_2 concentration data. *Environmental Research Letters*, *10*(3), 034012. Retrieved from `https://dx.doi.org/10.1088/1748-9326/10/3/034012` doi: 10.1088/1748-9326/10/3/034012

Schuldt, K. N., Mund, J., Luijkx, I. T., Aalto, T., Abshire, J. B., Aikin, K., ... van den Bulk, P. (2022). *Multi-laboratory compilation of atmospheric carbon dioxide data for the period 1957-2021; obspack_co2_1_globalviewplus_v8.0_2022-08-27.* NOAA Global Monitoring Laboratory. doi: 10.25925/20220808

Seneviratne, S., Zhang, X., Adnan, M., Badi, W., Dereczynski, C., Di Luca, A., ... Zhou, B. (2021). [Book Section]. In V. Masson-Delmotte et al. (Eds.), *Climate change 2021: The physical science basis. contribution of working group i to* *the sixth assessment report of the intergovernmental panel on climate change* (chap. Weather and Climate Extreme Events in a Changing Climate). Cambridge University Press, Cambridge, United Kingdom and New York, NY, USA: Cambridge University Press. doi: 10.1017/9781009157896.013

Shenoy, S., Gorinevsky, D., Trenberth, K. E., & Chu, S. (2022). Trends of extreme US weather events in the changing climate. *Proceedings of the National Academy of Sciences*, *119*(47), e2207536119. Retrieved from `https://www.pnas.org/doi/abs/10.1073/pnas.2207536119` doi: 10.1073/pnas.2207536119

Stanevich, I., Jones, D. B. A., Strong, K., Parker, R. J., Boesch, H., Wunch, D., ... Deng, F. (2020). Characterizing model errors in chemical transport modeling of methane: impact of model resolution in versions v9-02 of geos-chem and v35j of its adjoint model. *Geosci. Model Dev.*, *13*(9), 3839–3862. Retrieved from `https://gmd.copernicus.org/articles/13/3839/2020/` doi: 10.5194/gmd-13-3839-2020

Sun, Q., Zhang, X., Zwiers, F., Westra, S., & Alexander, L. V. (2021). A global, continental, and regional analysis of changes in extreme precipitation. *Journal of Climate*, *34*(1), 243 - 258. Retrieved from `https://journals.ametsoc.org/view/journals/clim/34/1/jcliD190892.xml` doi: 10.1175/JCLI-D-19-0892.1

Sun, Y., Frankenberg, C., Wood, J. D., Schimel, D., Jung, M., Guanter, L., ... others (2017). OCO–2 advances photosynthesis observation from space via solar-induced chlorophyll fluorescence. *Science*, *358*(6360), eaam5747.

Thompson, R. L., Broquet, G., Gerbig, C., Koch, T., Lang, M., Monteil, G., ... others (2020). Changes in net ecosystem exchange over europe during the 2018 drought based on atmospheric observations. *Philosophical Transactions of the Royal Society B*, *375*(1810), 20190512.

Turner, A. J., Köhler, P., Magney, T. S., Frankenberg, C., Fung, I., & Cohen, R. C. (2021). Extreme events driving year-to-year differences in gross primary productivity across the us. *Biogeosciences*, *18*(24), 6579–6588. Retrieved from `https://bg.copernicus.org/articles/18/6579/2021/` doi: 10.5194/bg-18-6579-2021

U.S. Energy Information Administration. (2023). *Energy-related co_2 emission data tables.* `https://www.eia.gov/environment/emissions/state/`. (Accessed 11 Aug 2023)

USDA-NASS. (2020). *Nass - quick stats.* USDA National Agricultural Statistics Service. Washington DC.

van der Werf, G. R., Randerson, J. T., Giglio, L., van Leeuwen, T. T., Chen, Y., Rogers, B. M., ... Kasibhatla, P. S. (2017). Global fire emissions estimates during 1997–2016. *Earth Syst. Sci. Data*, *9*(2), 697–720. Retrieved from `https://www.earth-syst-sci-data.net/9/697/2017/` doi: 10.5194/essd-9-697-2017

Wei, Y., Shrestha, R., Pal, S., Gerken, T., Feng, S., McNelis, J., ... others (2021). Atmospheric Carbon and Transport–America (ACT-America) data sets: Description, management, and delivery. *Earth and Space Science*, *8*(7), e2020EA001634. doi: 10.1029/2020EA001634

West, T. O., Bandaru, V., Brandt, C. C., Schuh, A. E., & Ogle, S. M. (2011). Regional uptake and release of crop carbon in the united states. *Biogeosciences*, *8*(8), 2037–2046. Retrieved from `https://bg.copernicus.org/articles/8/2037/2011/` doi: 10.5194/bg-8-2037-2011

West, T. O., Brandt, C. C., Baskaran, L. M., Hellwinckel, C. M., Mueller, R., Bernacchi, C. J., ... others (2010). Cropland carbon fluxes in the united states: Increasing geospatial resolution of inventory-based carbon accounting. *Ecological Applications*, *20*(4), 1074–1086.

Yin, Y., Byrne, B., Liu, J., Wennberg, P. O., Davis, K. J., Magney, T., … others (2020). Cropland carbon uptake delayed and reduced by 2019 midwest floods. *AGU Advances*, *1*(1), e2019AV000140.

Yu, K., Keller, C. A., Jacob, D. J., Molod, A. M., Eastham, S. D., & Long, M. S. (2018). Errors and improvements in the use of archived meteorological data for chemical transport modeling: an analysis using GEOS-Chem v11-01 driven by GEOS-5 meteorology. *Geosci. Model Dev.*, *11*(1), 305–319. Retrieved from https://www.geosci-model-dev.net/11/305/2018/ doi: 10.5194/gmd-11-305-2018

Yu, S., Falco, N., Patel, N., Wu, Y., & Wainwright, H. (2023, jun). Diverging climate response of corn yield and carbon use efficiency across the U.S. *Environmental Research Letters*, *18*(6), 064049. Retrieved from https://dx.doi.org/10.1088/1748-9326/acd5e4 doi: 10.1088/1748-9326/acd5e4

Zscheischler, J., Westra, S., Hurk, B. J. J. M. v. d., Seneviratne, S. I., Ward, P. J., Pitman, A., … Zhang, X. (2018). Future climate risk from compound events. *Nature Climate Change*, *8*(6), 469–477.

Regional inversion shows promise in capturing extreme-event-driven CO_2 flux anomalies but is limited by atmospheric CO_2 observational coverage

B. Byrne[1], J. Liu[1,2], K. W. Bowman[1,3], Y. Yin[2,*], J. Yun[1], G. D. Ferreira[4], S. M. Ogle[4,5], L. Baskaran[1], L. He[6], X. Li[7], J. Xiao[8], K. J. Davis[9]

[1]Jet Propulsion Laboratory, California Institute of Technology, Pasadena, CA, USA
[2]Division of Geological and Planetary Sciences, California Institute of Technology, Pasadena, CA, USA
[3]Joint Institute for Regional Earth System Science and Engineering, University of California, Los Angeles, USA
[4]Natural Resource Ecology Laboratory, Colorado State University, Fort Collins, CO 80523, United States of America
[5]Department of Ecosystem Science and Sustainability, Colorado State University, Fort Collins, CO 80523, United States of America
[6]Department of Global Ecology, Carnegie Institution for Science, Stanford, CA, United States of America
[7]Research Institute of Agriculture and Life Sciences, Seoul National University, Seoul, South Korea
[8]Earth Systems Research Center, Institute for the Study of Earth, Oceans, and Space, University of New Hampshire, Durham, NH, USA
[9]Department of Meteorology and Atmospheric Science, and Earth and Environmental Systems Institute, The Pennsylvania State University, University Park, Pennsylvania
*Now at Department of Environmental Studies, New York University, New York, NY, USA

Key Points:

- Bottom-up and top-down methods independently capture reduced 2019 US Midwest carbon uptake
- Gaps in atmospheric CO_2 observations drive uncertainties in top-down estimates
- Nested inversion better localizes US Midwest ΔNEE relative to coarse global model

Corresponding author: Brendan Byrne, brendan.k.byrne@jpl.nasa.gov

Corresponding author: Junjie Liu, junjie.liu@jpl.nasa.gov

Abstract

Extreme climate events are becoming more frequent, with poorly understood implications for carbon sequestration by terrestrial ecosystems. A better understanding will critically depend on accurate and precise quantification of ecosystems responses to these events. Taking the 2019 US Midwest floods as a case study, we investigate current capabilities for tracking regional flux anomalies with “top-down” inversion analyses that assimilate atmospheric CO_2 observations. For this analysis, we develop a regionally nested version of the NASA Carbon Monitoring System-Flux (CMS-Flux) that allows high resolution atmospheric transport ($0.5° \times 0.625°$) over a North America domain. Relative to a 2018 baseline, we find US Midwest growing season net carbon uptake is reduced by 11-57 TgC (3–16%) for 2019 (inversion mean estimates across experiments). These estimates are found to be consistent with independent “bottom-up” estimates of carbon uptake based on vegetation remote sensing. We then investigate current limitations in tracking regional carbon emissions and removals by ecosystems using “top-down” methods. In a set of observing system simulation experiments, we show that the ability to recover regional carbon flux anomalies is still limited by observational coverage gaps for both in situ and satellite observations. Future space-based missions that allow for daily observational coverage across North America would largely mitigate these observational gaps, allowing for improved top-down estimates of ecosystem responses to extreme climate events.

Plain Language Summary

Extreme climate events, such as floods or heatwaves, can have major impacts on the carbon cycle. For example, widespread flooding in the US Midwest during 2019 delayed the planting of crops leading to reduced plant growth and carbon uptake relative to 2018. Here, we test how well this reduction in carbon uptake can be inferred from measurements of atmospheric CO_2. We find that these data can identify reduced net carbon uptake to the US Midwest during the 2019 floods, but that sparse observational coverage limits our ability to quantify the anomaly in net carbon uptake.

1 Introduction

Extreme events, including heat and precipitation extremes, are becoming more frequent (Shenoy et al., 2022; Q. Sun et al., 2021; Kirchmeier-Young & Zhang, 2020; Seneviratne et al., 2021). These events have significant implications for carbon sequestration in terrestrial ecosystems, often causing carbon losses in a single year equal to many years of carbon sequestration (Ciais et al., 2005; Byrne et al., 2021). This is concerning because Nature-based Climate Solutions (NbCSs), which aim to enhance the terrestrial carbon sink through improved land management, have been proposed as an important tool to mitigate CO_2 emissions (Fargione et al., 2018). The increasing frequency of extreme events may disrupt this process, creating a carbon-climate feedback where extreme-event-driven carbon emissions reduce the effectiveness of NbCSs (Zscheischler et al., 2018; Barkhordarian et al., 2021). Consequently, there is an urgent need to quantify the impact of extreme events on carbon uptake by ecosystems for policy programs and other climate applications.

“Top-down” methods offer an approach for estimating biosphere-atmosphere CO_2 fluxes based on observations of atmospheric CO_2. Typically, Bayesian inverse methods are used to estimate optimal surface fluxes based on constraints from prior information and atmospheric CO_2 observations. Although historically data limited, these techniques are increasingly used to quantify regional carbon cycle responses to extreme events, thanks to expansions of in situ CO_2 measurements and the introduction of space-based retrievals of column-averaged dry-air CO_2 mole fractions (X_{CO_2}) from missions like the Orbiting Carbon Observatory 2 (OCO-2) (Feldman et al., 2023; Byrne et al., 2021). Still, current capabilities for tracking extreme events are not well understood. This study aims to improve our characterization of these capabilities and identify current limitations.

As a case study, we examine the 2019 US Midwest floods. Intense precipitation during that spring ($> 2\sigma$ above average) led to widespread flooding across the US Midwest, a region that accounts for 40% of world corn and soybean production (Yin et al., 2020). Inundation delayed crop planting by 2–3 weeks relative to 2018 across the region, with an additional reduction of 6.8 million hectares in the total planted area. These factors led to a 16-day shift in the seasonal cycle of photosynthesis relative to 2018, along with a 15% lower peak value (Yin et al., 2020). In turn, crop yields across the US Midwest were reduced by ~14%, and a decrease in net carbon uptake of ~0.1 PgC was inferred relative to the preceding years (Yin et al., 2020; Balashov et al., 2022). The relatively simple (delayed planting) and well documented carbon cycle perturbation during this event makes it an ideal case study for studying our ability to quantify carbon cycle perturbations using top-down and bottom-up methods.

To perform our analysis, we introduce a regionally nested version of the CMS-Flux inversion system with high-resolution ($0.5°\times0.625°$) atmospheric transport over North America (see Sec. 2.1). This version offers advantages over the coarse-resolution ($4°\times 5°$) global version of CMS-Flux. It reduces transport errors introduced by the coarsening of reanalysis winds (Stanevich et al., 2020; K. Yu et al., 2018) and better represents assimilated CO_2 observations, resulting in improved localization of extreme-event-driven CO_2 flux anomalies (Sec. 3.2.2).

The first objective of this study is to evaluate how well existing atmospheric observing systems can quantify flood-induced reductions in carbon uptake during 2019 relative to 2018. We conduct four inversions that assimilate (1) in situ CO_2 measurements (IS), (2) OCO-2 land X_{CO_2} retrievals (LNLG), (2) both insitu and OCO-2 land data (LNLGIS), or (4) in situ, OCO-2 land and ocean data (LNLGOGIS)(Sec. 2.1). Climatological prior fluxes are employed in each experiment, allowing us to attribute posterior anomalies in carbon uptake between years solely to the assimilation of atmospheric CO_2 data. We then compare these estimates with an independent ensemble of remote-sensing bottom-up estimates and with crop-yield data to assess their overall consistency (Sec. 3.1).

The second objective of this study is to assess the impact of existing observational coverage gaps and the potential expansion of space-based X_{CO_2} measurements on our ability to detect extreme-event-driven anomalies in CO_2 fluxes. To evaluate the effect of expanded space-based observations, we devise a hypothetical observing system that provides daily X_{CO_2} retrievals at 13:00 local time (similar to OCO-2). Subsequently, we conduct observing system simulation experiments (OSSEs) for existing in situ data and OCO-2 data as-well as the hypothetical observing system. For each OSSE, we evaluate the effectiveness in capturing extreme-event-driven CO_2 flux anomalies (Sec. 3.2.1). Our aim is to gain a deeper understanding of how observational coverage impacts our ability to quantify the influence of extreme events on CO_2 fluxes.

2 Methods

Sec. 2.1 introduces the configuration for the nested North America version of the CMS-Flux atmospheric CO_2 inversion system, including its application for real data experiments (Sec. 2.1.1) and OSSEs (Sec. 2.1.2). Sec. 2.2 describes remote-sensing bottom-up NEE anomaly estimates used in this study. Sec. 2.3 describes the state crop production estimates.

2.1 Top-down ΔNEE estimate

We establish a one-way nested inversion system covering the North America region, spanning from 40°W to 167.5°W and 14°N to 76°N. Within this domain, model transport is conducted at a spatial resolution of 0.5° × 0.625° with a five-minute timestep, using archived MERRA-2 reanalysis data. We employ four-dimensional variational data assimilation (4D-Var) to optimize scaling factors on prior land and ocean fluxes. These fluxes are optimized at a coarser spatial and temporal resolution compared to the nested model transport. Spatially, a mask is applied to optimize fluxes over a 4°×5° grid, which is truncated at the land-ocean boundary. Temporally, we utilize a six-week inversion window and optimize weekly mean land and ocean scaling factors. The middle four weeks of the inversion window are retained as optimized fluxes, while the first and last weeks are excluded as spin-up and spin-down periods. We conduct a batch of eight six-week inversions offset by four weeks, yielding continuous fluxes from April 8th to November 18th for both 2018 and 2019, resulting in a total of 16 inversion runs.

For each experiment, the nested inversion setup is run three times using different prior fluxes (the BCs and ICs also differ for the real-data experiments, see Sec. 2.1.1). The prior NEE fluxes are derived from the posterior NEE fluxes of the GOSAT+surface+TCCON experiment by Byrne et al. (2020) and differ based on the employed prior NEE (CASA, SiB3, or FLUXCOM). A climatological seasonal cycle is calculated for each prior NEE flux over the period of 2010-2015. Subsequently, the climatological NEE seasonal cycle is partitioned into net primary production (NPP) and heterotrophic respiration (HR) components by subtracting the 2010-2015 mean seasonal cycle from the mean bottom-up NPP estimate (assumed to be 65% of mean GPP estimate here). In the inversions, we impose both the NPP and HR fluxes in the forward simulation, but optimize scaling factors only on the weekly mean HR fluxes. This choice is driven by the improved performance of this configuration during the spring and fall when NEE is close to zero, requiring large scaling factors to adjust the NEE flux. The posterior HR fluxes are not interpreted independently but combined with the prior NPP fluxes to obtain a posterior estimate of NEE for analysis. We generate prior uncertainties on the HR fluxes based on the full range of the three prior NEE fluxes. Prior ocean fluxes are derived similarly from the posterior ocean flux estimates of the GOSAT+surface+TCCON experiment by Byrne et al. (2020), and uncertainties on these estimates reflect the range among the three experiments that employ different NEE priors. The prior fluxes, posterior fluxes, and associated uncertainties are provided as supporting information.

In addition to the ocean, NPP, and HR fluxes, the forward simulations incorporate prescribed fossil fuel emissions, biomass burning emissions, biofuel emissions, and diurnal NEE. Fossil Fuel emissions used here were specifically made for the v10 OCO-2 modelling intercomparison project (MIP) (Byrne et al., 2023; Basu & Nassar, 2021). Biomass burning emissions are derived from the Global Fire Emissions Database version 4 (GFED4.1s) and scaled to incorporate diurnal variations in emissions (van der Werf et al., 2017). Biofuel emissions are obtained from the CASA-GFED4-FUEL dataset. Diurnal variations in NEE are based on the diurnal NEE variations from the CASA and SiB3 models, as described in Byrne et al. (2020). The SiB3 diurnal cycle is employed for the SiB3-based and FLUXCOM-based NEE priors, while the CASA diurnal cycle is prescribed for the CASA-based inversion. All of these fluxes are regridded from their native spatial resolution to 0.5°×0.625° (fossil fuel emissions were at 1.0°×1.0° degrees, biomass burning emissions were at 0.25°×0.25° degrees, and remaining fluxes were at 4° × 5° as archived by Byrne et al. (2020)).

2.1.1 Real data experiment

First, we require atmospheric CO_2 boundary and initial conditions for the nested model. To generate these conditions, we conduct a global 4°×5° 4D-Var inversion that optimizes scaling factors on prior land and ocean fluxes. These global inversions utilize the same configuration as Byrne et al. (2020). The resulting optimized global NEE and ocean fields are then employed in a $2° \times 2.5°$ global simulation to produce boundary conditions and initial conditions for the nested domain. The global inversions are performed three times, corresponding to each of the three prior NEE estimates. The nested inversion setup is subsequently executed three times using the three different prior fluxes, boundary conditions, and initial conditions based on the three distinct prior flux estimates.

Four sets of experiments are conducted, differing in the assimilated data. The "IS" experiment assimilates in situ CO_2 measurements from the global network of sites as described below. The "LNLG" experiment assimilates OCO-2 land data, including nadir and glint retrievals. The "LNLGIS" experiment assimilates both in situ and OCO-2 land data. Lastly, the "LNLGOGIS" experiment assimilates in situ, OCO-2 land data, and OCO-2 ocean glint retrievals.

In situ CO_2 measurements are obtained from version 8.0 of the NOAA GLOBALVIEW plus Obspack dataset (Schuldt et al., 2022). These data are provided on the X2019 CO_2 scale but were back corrected to the X2007 CO_2 scale following Hall et al. (2021). We apply several filters to the in situ data before assimilation. Surface in situ CO_2 measurements are assimilated at their respective height above the surface, with inclusion criteria that the model surface elevation should differ by less than 500 m from the 15 arc-second ETOPO1 global elevation dataset (NOAA, 2021). Secondly, we only assimilate data with the CT_assim flag greater than or equal to one, which indicates data that is deemed assimilable for the NOAA CarbonTracker system. Finally, only measurements obtained between 11:00 and 17:00 local time are assimilated (when the atmospheric boundary layer is well mixed). The sites assimilated are: amt, bck, bmw, bra, brw, cba, cby, chl, cps, crv, egb, esp, est, etl, fsd, inu, inx, key, kum, lef, lew, llb, sct, sgp, uta, wbi, wgc, wkt, wsa. The sites with CT_assim$\geq$ 1 that are not assimilated are: mbo, mex, mlo, mwo, nwr, omp, uts, wsd. We note that some sites with CT_assim= 0 may be assimilable, but more work is needed to characterize their suitability for assimilation. We apply the CT_MDM "model-data-mismatch" values as uncertainties on assimilated measurements. All aircraft data, including the ACT-America campaign data (Davis et al., 2021, 2018; Wei et al., 2021), are withheld for validation purposes. Monthly maps of data density are shown in Figure S1.

We employ X_{CO_2} retrieved using version 10 of NASA's Atmospheric CO_2 Observations from Space (ACOS) full-physics retrieval algorithm (O'Dell et al., 2018). Subsequently, OCO-2 "buddy" super-observations are calculated by averaging individual soundings into super-observations at a spatial resolution of $0.5° \times 0.5°$ within the same orbit, assigning equal weights, following the approach by Liu et al. (2017). Monthly maps illustrating data density are shown in Figure S2.

The global inversions discussed in Sec. 3.2.2 follow an identical set-up as the nested inversions, with the same flux datasets regrided to $4° \times 5°$ globally.

2.1.2 Observing System Simulation Experiments

A series of OSSEs are conducted to explore the impact of observational coverage in quantifying carbon cycle perturbations resulting from extreme events. These OSSEs cover the same two year period as the real data inversions. Four OSSE experiments are carried out: IS, LNLG, LNLGOGIS, and one for a new hypothetical space-based observing system that provides daily X_{CO_2} retrievals at 13:00 (1 pm). This hypothetical system, referred to as the ideal LEO mission, could comprise a dense constellation of low Earth orbit (LEO) sensors. The OSSEs are carried out following the same setup as the real data experiments, while the true atmospheric CO_2 boundary and initial conditions are implemented for the nested inversion.

For the ideal LEO mission, pseudo-observations are generated as follows: 1 pm observations within each land 0.5°×0.625° grid cell are filtered to exclude instances of low-light conditions, cloudy conditions, and when the surface is covered by snow or ice. Fractional snow cover and cloud cover data are obtained from the MERRA-2 reanalysis dataset (Gelaro et al., 2017). Measurements are excluded for grid cells with a fractional area of land snow cover (FRSNO) greater than 75% and total cloud area fraction (ISCCPCLD-FRC) greater than 75% from the International Satellite Cloud Climatology Project (ISCCP). Additionally, observations with an atmospheric path exceeding six air-masses are removed. We allow one super-obs within each gridcell per day. The uncertainty on the super-obs is defined to be 0.7 ppm, roughly matching OCO-2. Monthly maps of data density for the ideal LEO mission are shown in Fig. S3.

True NEE fluxes for the OSSEs are generated by combining a climatological NEE seasonal cycle with anomalies from the bottom-up datasets. Climatological true NEE fluxes are obtained from the CASA-GFED3 model, which undergoes downscaling from monthly to three-hourly fluxes. These fluxes align with those described in Appendix 3 of Byrne et al. (2020). Interannual variations in the true fluxes are introduced by incorporating NEE anomalies taken to be 65% of the mean bottom-up GPP anomalies across the five datasets (see Sec. 2.2). Pseudo-observations are then generated by conducting a forward simulation using the nested model.

2.2 Remote-sensing bottom-up ΔGPP and ΔNEE estimates

We generate an ensemble of five bottom-up ΔGPP estimates by combining a number of remote-sensing-based GPP datasets. Four of these are obtained from existing datasets: 8 day FLUXCOM remote-sensing-based (RS) GPP (Jung et al., 2020), FluxSat Version 2 (Joiner & Yoshida, 2020), GOSIF GPP (Li & Xiao, 2019), and the NIR_V-based GPP estimates of L. He et al. (2022). All of these data are regridded from their native resolution to weekly temporal resolution and 0.5° × 0.625° spatial resolution.

In addition, we estimate GPP directly from TROPOMI SIF data. This followed the same approach as Yin et al. (2020). Two GPP estimates are then calculated using land-cover-dependent SIF-to-GPP scaling factors from Li et al. (2018) and Y. Sun et al. (2017), which were adjusted by a factor of 0.64 to account for difference retrieval wavelegnths between OCO-2 and TROPOMI (740 nm vs 757 nm). These factors were then applied to gridded SIF data (0.08333° spatial and 8 day temporal resolution), while accounting for the fractional vegetation cover within each gridcell. The GPP estimates were then regridded to 0.5°×0.625° spatial resolution. Any data gaps within the growing season are then filled by linear interpolation over time, while GPP is assumed to be zero for data gaps outside the growing season. Finally the two GPP estimates are averaged.

From these GPP datasets, we estimate an anomaly in NEE between 2018 and 2019 by assuming the NEE anomaly is equal to the NPP anomaly, which is itself related to the GPP anomaly by:

$$\Delta\text{NEE} = -\Delta\text{NPP} = -0.60 \times \Delta\text{GPP} \tag{1}$$

The factor of 0.60 is an estimate of the carbon use efficiency (CUE), and is a relatively high estimate (Manzoni et al., 2018; Y. He et al., 2018), though may be representative of corn (S. Yu et al., 2023; Campioli et al., 2015). We assume an error of ±0.1 in CUE, and perform error analysis using factors of 0.5 and 0.7. The conversion of ΔNPP to ΔNEE assumes that ΔHR is negligible. This is likely a poor assumption, but a limitation of remote-sensing estimates that are insensitive to HR variations. Previously, Yin et al. (2020) showed that bottom-up ΔNEE estimated assuming negligible ΔHR could reasonably reproduce observed atmospheric CO_2 enhancements during the 2019 US Midwest floods, providing some evidence that ΔHR variations have a secondary impact.

2.3 State crop yields and NPP

Crop yields, which represents the amount of crop biomass removed from the field during harvest events, have been estimated using county-level crop yield data from the US Department of Agriculture (USDA) - National Agricultural Statistics Service (NASS) (USDA-NASS, 2020). The carbon content of crop yields was derived from the relationship:

$$\mathrm{Y_C} = \mathrm{Y_{NASS}} \times \mathrm{DM} \times \mathrm{C_f}, \tag{2}$$

where $\mathrm{Y_C}$ is the crop yield, in units of carbon, $\mathrm{Y_{NASS}}$ is the annual county-level crop yield data from USDA-NASS, DM is the dry matter content for each crop, and $\mathrm{C_f}$ is carbon content crop factor. Crop NPP ($\mathrm{NPP_{crop}}$), representing the net carbon uptake by crops, was derived from the crop yield estimates using the following equation:

$$\mathrm{NPP_{crop}} = \mathrm{Y_{NASS}} \times \frac{1}{\mathrm{HI}} \times (1 + \mathrm{R_{RS}}) \times \mathrm{DM} \times \mathrm{C_f}, \tag{3}$$

where HI is the harvest index for each crop, i.e., the proportion of harvested material (e.g., grains) in relation to total crop aboveground biomass; and RRS is the root:shoot ratio for each crop. We used crop-specific factors for dry matter, root:shoot ratios, harvest indices, and carbon content following the methods in West et al. (2010, 2011) and Ogle et al. (2015). Crop yields and NPP were estimated for over 20 crops, which together represented >99% of total US crop production (USDA-NASS, 2020). Uncertainty in estimates were propagated through a Monte Carlo approach with 10,000 replicates and probability distribution functions for all input data and factors. The results are based on the mean and 95% confidence intervals from the final distribution of simulated values. We note that NASS only included uncertainty in crop yield data for 2020 so we assumed a similar level of uncertainty in crop yields for the other years.

3 Results

3.1 Flood-induced NEE anomalies

Figure 1a–b illustrates the difference in June-July NEE between 2019 and 2018 ($\Delta\mathrm{NEE} = \mathrm{NEE_{2019}} - \mathrm{NEE_{2018}}$) for both the remote-sensing bottom-up (ensemble mean) and top-down (LNLGOGIS) estimates. The analyses reveal a significant decrease in CO_2 uptake (positive ΔNEE) specifically in the US Midwest region. This pronounced positive ΔNEE signal in the US Midwest stands out compared to the rest of the continent. Figure 1c presents the 5 week running mean time series of ΔNEE over the US Midwest. Both the top-down and bottom-up estimates depict a positive ΔNEE signal throughout Jun–Jul, with the anomaly peaking towards the end of June. However, during Aug-Sep, the top-down and bottom-up estimates suggest a negative ΔNEE in the US Midwest. Across the rest of the continent (Figure 1d), anomalies are weaker. The top-down estimate suggests a positive anomaly outside the US Midwest during August, while the bottom-up estimate suggests no significant anomalies. The supplementary materials display the maps and timeseries for the other top-down experiments (Fig. S4) and individual bottom-up datasets (Fig. S5).

Figure 2 shows US Midwest ΔNEE for each of the top-down and bottom-up estimates. In addition, an estimate of the anomaly in net primary production for crops ($\Delta\mathrm{NPP_{crop}}$) derived from crop yield data is shown. All estimates suggest positive ΔNEE over the study period (-6–85 TgC for top-down, 15–78 TgC for bottom-up, and 36–65 TgC for yield-based estimates). We find that June-July ΔNEE drives the annual anomaly with uptake reduced by 24–76 TgC in top-down estimates and 38–131 TgC in bottom-up estimates. The bottom-up estimates suggest this is moderated when integrating across the growing season due to greater carbon uptake during Aug-Sep (-56 TgC to -15 TgC), while the top-down estimates are less consistent during Aug-Sep, ranging from -37 TgC to 34 TgC. Figure S6 demonstrates that the bottom-up and top-down ΔNEE generally show similar June-July ΔNEE across the CONUS Climate Assessment Regions. In particular, we

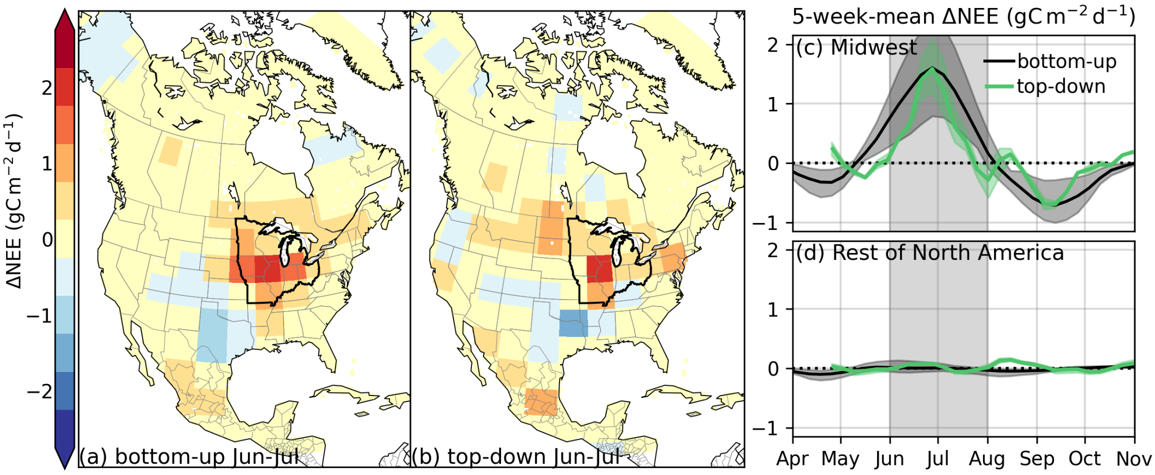

Figure 1. (a) Bottom-up and (b) top-down (LNLGOGIS) spatial patterns of June–July mean ΔNEE ($NEE_{2019} - NEE_{2018}$) at 4° × 5° spatial resolution. (c) US Midwest and (d) rest of North America 5-week-mean ΔNEE. The US Midwest is defined as the area within Illinois, Indiana, Iowa, Michigan, Minnesota, Missouri, Ohio, and Wisconsin and is indicated by the black outline in panels (a) and (b). The shading shows the range around the mean estimate for the inversions using three different priors and for the five bottom-up GPP datasets.

find that all estimates obtain negative ΔNEE across the Southern Great Plains (-22 to -46 TgC), resulting from the 2018 drought (Turner et al., 2021).

These findings suggest that both in situ and OCO-2 data provide adequate observational coverage to detect the June-July ΔNEE signal resulting from the 2019 US Midwest floods. However, some differences are also evident. The experiments disagree in the sign of Aug-Sep ΔNEE. The IS experiment shows negative Aug-Sep ΔNEE that largely compensates for the positive June–July ΔNEE. Conversely, the LNLG experiment gives positive Aug–Sep ΔNEE but the smallest June–July ΔNEE. There are some spatial differences as-well, for example, the IS experiment suggests larger positive ΔNEE in western Canada and negative ΔNEE in the southeast during Jun-Jul than the other experiments (Fig. S4). The LNLGIS and LNLGOGIS experiments yield quite similar results. The relative accuracy of these different estimates is challenging to evaluate, as a number of different drivers could contribute to differences but all experiments exhibit good agreement with independent aircraft CO_2 measurements during 2018 and 2019 (Text S1, Fig. S7-S12). The disparities between experiments may arise from differences in observational coverage and this hypothesis is examined in Sec. 3.2.1.

The bottom-up estimates show some notable differences in the magnitude of ΔNEE over the US Midwest and the spatial structure of ΔNEE outside the US Midwest (Fig. S5). FLUXCOM consistently displays the weakest ΔNEE signal, and has been previously shown to underestimate interannual variations in NEE and GPP (Jung et al., 2020). Outside the US Midwest, the NIR_V-based estimate shows negative values across the western half of North America, which are not observed in any other estimates, while the TROPOMI-based estimate indicates positive ΔNEE across a large portion of eastern Canada. Consequently, the net June–July ΔNEE signal outside the US Midwest varies across datasets, ranging from -218 TgC to 187 TgC.

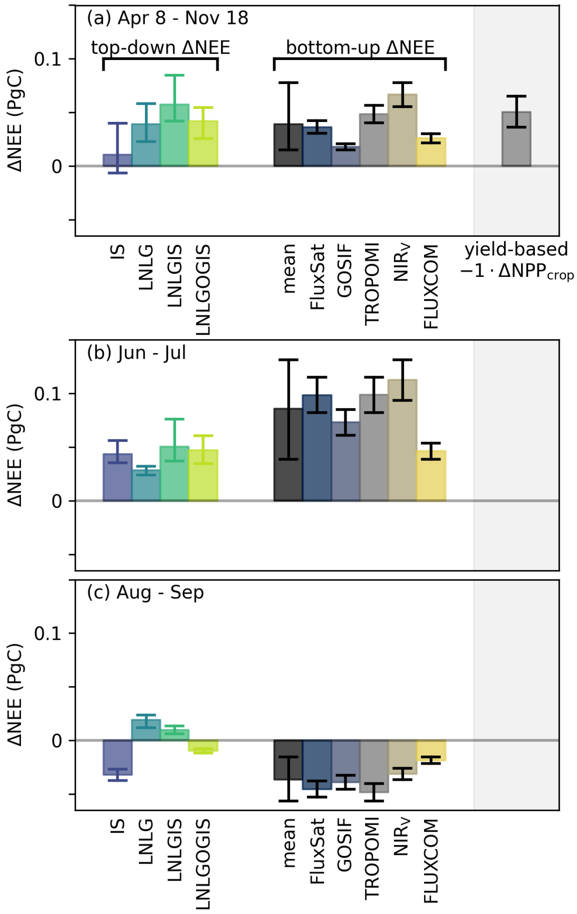

Figure 2. Top-down ΔNEE, bottom-up ΔNEE, and yield-based ΔNPP for crops (ΔNPP_{crop}) over the US Midwest. ΔNEE is calculated for (a) the entire inversion period (April 8th – Nov 18th), (b) June-July and (c) Aug-Sep. The top-down estimates show the mean and range obtained using three different priors. Uncertainty bars for the top-down estimates show the range using three priors, while the uncertainties on the bottom-up show the range of using carbon use efficiencies of 0.5–0.7.

3.2 Sensitivity experiments

3.2.1 Impact of observational coverage

Although both the in situ network and OCO-2 were able to identify a positive US Midwest ΔNEE signal, we found substantial differences between the top-down experiments. Here we perform OSSEs to investigate whether gaps in observational coverage could explain these differences. Further, we test whether increased observational coverage (in an ideal LEO constellation) would substantially improve top-down estimates of extreme-event-driven carbon cycle perturbations.

Figure 3 shows the true and posterior ΔNEE for the OSSEs. All OSSEs recover positive ΔNEE to the US Midwest, consistent with the real data experiments. However, June-July US Midwest ΔNEE is underestimated by 43% for IS, 75% for LNLG, 48% for LNLGOGIS and 15% for the ideal LEO constellation. In addition, the inversions tend to introduce a positive June–July ΔNEE outside the US Midwest that is not present in the truth. Over June-July, the true continental-scale ΔNEE is 89 TgC, while the mean inversion estimates are 163 TgC (error of +74 TgC) for IS, 93 TgC (error of +4 TgC) for LNLG, 68 TgC (error of -21 TgC) for LNLGOGIS, and 93 TgC (error of +4 TgC) for ideal LEO. A similar large continental-scale positive June–July ΔNEE was found for the real data IS experiment (Fig. S4ci). One possible explanation is that the limited spatial coverage of the in situ (Fig. S1) data may limit the ability to capture aggregate continental-scale budgets using a one-way nested system.

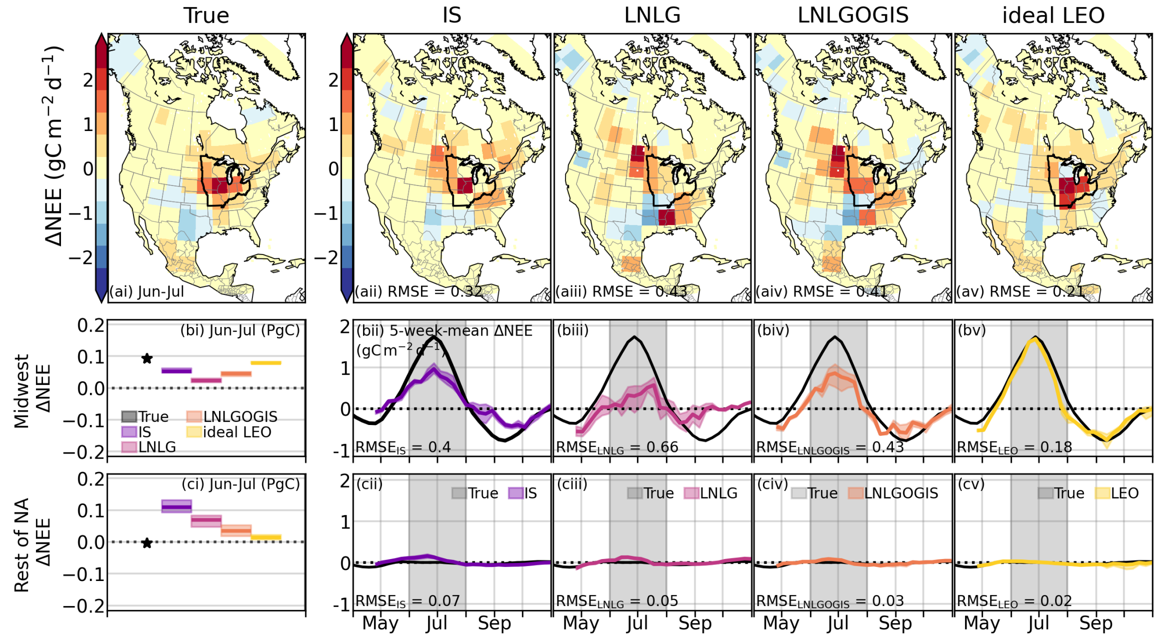

Figure 3. ΔNEE estimates for the OSSEs. Panel (ai) shows the true June-July ΔNEE maps, while panels (aii)–(av) show the OSSE posterior June-July ΔNEE maps and RMSE across gridcells (gC m^{-2} d^{-1}). The net US Midwest Jun-Jul ΔNEE (PgC) is shown for each OSSE in panel (bi), and the timeseries of 5-week-mean ΔNEE is shown for each experiment in panels (bii)–(bv), with RMSE across weeks (gC m^{-2} d^{-1}). The same quantities are show for the rest of North America in panels (ci)–(cv).

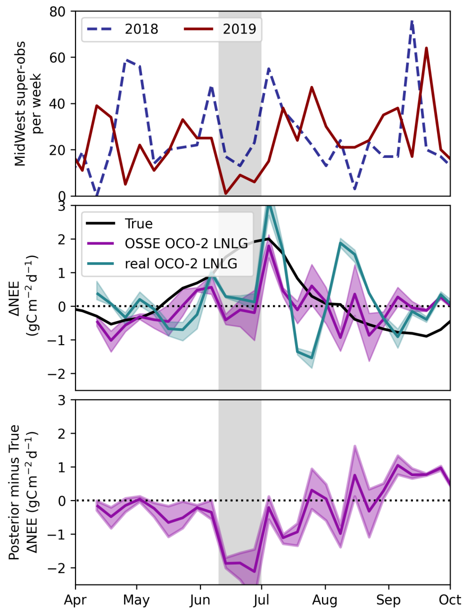

Figure 4. Weekly timeseries of (top) number of OCO-2 super-obs in the US Midwest for 2018 and 2019. (middle) Weekly ΔNEE in the US Midwest for the truth, OCO-2 OSSE and real OCO-2 LNLG experiment. (bottom) Difference between posterior and true ΔNEE for the OCO-2 OSSE. The shading shows the range around the mean estimate for the inversions using three different priors.

Overall, the LNLG OSSE shows the worst performance at isolating the US Midwest ΔNEE. We suggest that this could be related to interannual variations in the observational coverage. Figure 4a shows that the number of LNLG weekly samplings over the US Midwest can be quite variable from year to year. In particular, there are only 16 super-obs in the US Midwest during the three week period of June 11, 2019 to July 2 2019. This coincides with near zero ΔNEE for both the real data LNLG inversion and OSSE (Fig. 4b), and the period with the largest error in ΔNEE for the OSSE (Fig. 4c). These results suggest that data gaps in OCO-2, particularly differences in observational coverage between years, limit our ability to estimate inter-annual variations in NEE at high spatio-temporal resolution.

The increased sampling from combining the datasets (LNLGOGIS) appears to moderately improve performance, particularly in isolating June–July ΔNEE to the US Midwest (relative to LNLG) and better capturing the continental-scale ΔNEE (relative to IS). However, the ideal LEO constellation results in much improved performance in both space and time. The ideal LEO constellation reduces June-July RMSE across $4° \times 5°$ regions by 34–51% and the 5-week-mean ΔNEE US Midwest RMSE by 55–73%. This comparison suggests that top-down estimates of extreme-event-driven perturbations to carbon uptake remain observationally-limited and that expanded space-based observing systems will improve these estimates.

3.2.2 Comparison between nested and global inversions

The nested CMS-Flux inversion system in this study offers both advantages and disadvantages compared to a global CMS-Flux inversion system. One major advantage is the ability to run transport at a higher resolution ($0.5° \times 0.625°$) compared to the global

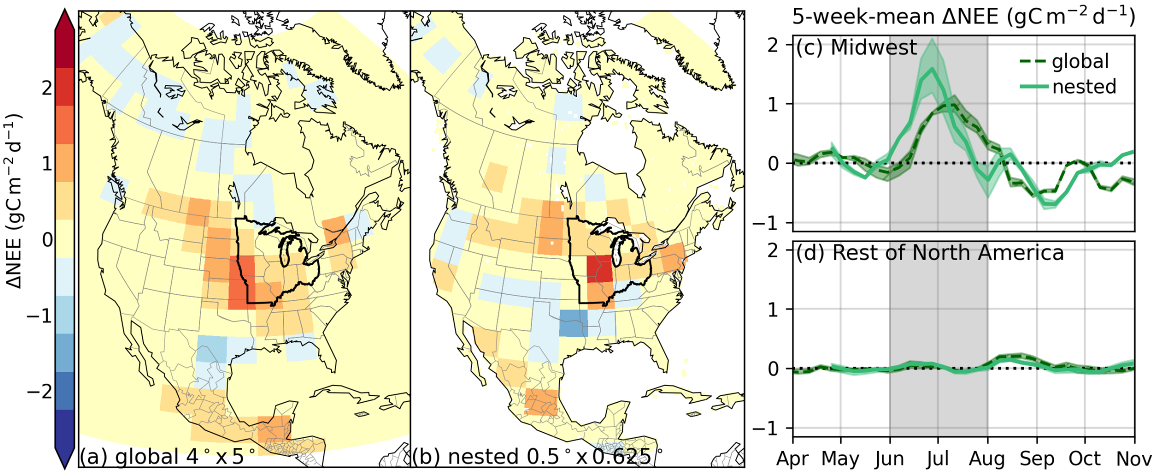

Figure 5. Comparison of the global 4° × 5° and nested inversion results. Maps of June–July ΔNEE from the LNLGOGIS experiment are shown for (a) the global 4° × 5° inversion and (b) the nested inversion. Weekly ΔNEE in the US Midwest after applying a 5-week running mean are also show for (c) the US Midwest and (d) rest of North America.

system (4°×5°). This higher resolution enables tracer transport to be closer to the parent model, as spatial averaging of meteorological fields can average out eddy transport, particularly affecting vertical motions (Stanevich et al., 2020). Additionally, a higher resolution model grid reduces representativeness errors, allowing better representation of fine-scale features that influence observations, such as topography. The primary disadvantage of the one-way nested system used in this study is the assumption of perfect boundary conditions and the inability to assimilate atmospheric CO_2 observations outside the nested domain. In a global inversion, fluxes over North America would impact measurements downwind, providing a powerful constraint on large-scale fluxes, including the net North American flux (Liu et al., 2015). A bias in flux at the continental scale would affect CO_2 fields across the entire Northern Hemisphere. Since the nested inversion lacks this constraint, significant errors in continental-scale fluxes may go undetected. Furthermore, biases in the imposed boundary CO_2 fields can propagate into optimized fluxes.

In order to assess the performance of the one-way nested inversion, we compare the obtained ΔNEE with the global version of CMS-Flux using the same inversion configuration, whenever possible. Figure 5 presents the results for both the global and nested versions of CMS-Flux. It is observed that the nested version of CMS-Flux effectively isolates ΔNEE to the US Midwest region during June–July. In contrast, the global model exhibits spatially broader positive ΔNEE across the US Midwest and Great Plains, resulting in a significantly reduced ΔNEE estimate for the US Midwest during June–July. The spatial pattern of ΔNEE for the nested model aligns more closely with the bottom-up estimate, suggesting that this system better captures the overall event. This indicates that, considering the observational coverage provided by LNLGOGIS, the benefits of reduced transport and representativeness errors in the nested model outweigh the detrimental impact of a limited domain.

We note that achieving good performance with nested version of CMS-Flux was challenging, and required a number of trial-and-error inversions. This included varying the size of the state vector spatially (0.5°×0.625° versus 4°×5° grid) and temporally (weekly, bi-weekly, monthly intervals). It also involved adjusting the prior constraints (optimizing HR rather than NEE, adjusting prior uncertainties). We suggest that these challenges are due to greater regularization requirements for the nested model in comparison to the global model. The sensitivities of observations to surface fluxes are limited to 1–2 weeks by the one-way nesting, such that large-scale constraints are imposed by the boundary conditions (Feng, Lauvaux, Davis, et al., 2019; Feng, Lauvaux, Keller, et al., 2019). Thus, the flux signal in the domain is generally much smaller than for the global model, where downwind observations provide important information for upwind continental-scale regions (Liu et al., 2015). We suggest that imposing an error correlation length between state-vector elements may be an effective approach for regularization in a nested inversion context (see Sec. 4.1), however, this is beyond the scope of our current study.

4 Discussion and Conclusions

Both top-down and bottom-up approaches capture a flood-induced reduction in net carbon uptake during the 2019 US Midwest floods. The top-down approach gave mean estimates of 11 TgC (IS), 39 TgC (LNLG), 57 TgC (LNLGIS), 42 TgC (LNLGOGIS) for US Midwest growing season ΔNEE. Meanwhile, the bottom-up datasets gave a mean estimate of 39 TgC (range: 15–78 TgC). These magnitudes are significant compared to anthropogenic emissions, amounting to as much as 28% of the US Midwest's annual fossil fuel emissions (300 $\mathrm{TgC\,yr^{-1}}$ for 2019, U.S. Energy Information Administration (2023)). In addition, this anomaly is comparable to the year-to-year variations in fossil fuel emissions (SD: 25 $\mathrm{TgC\,yr^{-1}}$), even including the reduction of regional emissions by 36 $\mathrm{TgC\,yr^{-1}}$ due to COVID-19 lockdowns in 2020.

In the context of more frequent heat and precipitation extremes (Seneviratne et al., 2021), accurate estimates of the carbon cycle responses will be critical for monitoring carbon budgets and evaluating carbon-climate feedbacks. The results of this study show that both top-down and bottom-up approaches demonstrate skill in capturing ΔNEE resulting from the 2019 Midwest floods, however a number of deficiencies were also identified. In the following sub-sections, we highlight current challenges and opportunities in quantifying carbon cycle extremes.

4.1 Top-down

Observational gaps in atmospheric CO_2 observations are identified as a key limitation in applying top-down methods to quantify extreme-event-driven ΔNEE, consistent with recent studies of the European carbon budget (W. He et al., 2023; Munassar et al., 2022; Monteil et al., 2020; Thompson et al., 2020). Through a series of OSSE experiments, it was demonstrated that gaps in both the in situ network and OCO-2 sampling impact the accuracy of ΔNEE estimates. While assimilating these two datasets concurrently partially mitigates the issue, fully resolving the problem requires expanded observations. Coverage similar to the ideal LEO observing system could be developed by combining multiple individual satellites, and motivates future studies that assimilate X_{CO_2} retrievals from multiple space-based observing systems concurrently (e.g., GOSAT, OCO-2, and OCO-3). In addition, efforts should be made to ensure consistency in X_{CO_2} retrievals between existing and planned missions (e.g., CO2M, GOSAT-GW). Expanding the in situ network would also likely enhance the ability to capture regional flux anomalies more effectively, however, this was not specifically explored.

Although current observing gaps are found to be a major limitation, there may be approaches to better regularize the inverse problem and reduce the impact of these gaps. In particular, applying off-diagonal co-variances in the prior error covariance matrix could be employed to adjust fluxes where observations are missing (Chen et al., 2023). Applying spatial co-variances will likely be especially important for in situ inversions, while applying temporal co-variances may be most useful for OCO-2 X_{CO_2} inversions. Of course, such an approach will only improve flux estimates if spatial and temporal co-variances are truly present, such that this approach will be limited by a correlation length scale. In addition, imposing realistic prior IAV could also be a fruitful approach, as has been done in previous studies evaluating the 2019 US Midwest floods (Yin et al., 2020; Balashov et al., 2022). However, high-confidence is needed in imposed prior IAV, as inaccurate prior IAV can significantly degrade posterior IAV estimates (Byrne et al., 2019). Text S2 and Figs. S13-15 show that imposing bottom-up IAV in the prior results in larger posterior ΔNEE anomalies during the Midwest Floods for all experiments. This is consistent with the ΔNEE anomalies being underestimated when using climatological priors, as was found in the OSSEs.

Finally, this study investigated the utility of a one-way nested version of CMS-Flux with $0.5°\times0.625°$ spatial resolution relative to the global model at $4°\times5°$ degree spatial resolution. We note that developing a nested inversion system involved considerable effort in tuning the state vector structure, assimilation window, and prior constraints. Nevertheless, we found that the nested model better allocated flood-induced ΔNEE to the US Midwest, suggesting that the improved model transport and observation representation of the nested model improved the overall performance relative to the global model, consistent with several recent studies (Monteil et al., 2020; Hu et al., 2019). However, the nested model has some disadvantages, especially the inability to assimilate downwind observations outside the model domain that may limit the utility of the nested model in other applications. Transport uncertainty and boundary condition errors may lead to significant challenges for nested inversions (Munassar et al., 2023; Kim et al., 2021; Chen et al., 2019; Lauvaux et al., 2012), but were not obvious in our analyses. We note that high-resolution models will be needed to take advantage of upcoming wide-swath sampling missions, such as CO2M (∼250 km swath) or GOSAT-GW (∼400 km swath).

4.2 Bottom-up

Remote-sensing-based bottom-up estimates of ΔNEE provided a consistent picture of reduced net uptake during the 2019 Midwest floods but differed significantly in magnitude. The primary source of this variability stems from translating space-based reflectance or SIF observations to GPP, leading to a range in ΔGPP between datasets of 120% of the mean. Indeed, estimating the magnitude of GPP from remote sensing datasets is challenging due to satellite signals that could be influenced by factors such as cloud coverage and soil background, in addition to calibration that is predominantly relying on benchmarks provided by eddy covariance sites. We encourage research into approaches that can reduce uncertainties on large-scale GPP magnitudes, possibly through top-down constraints from Carbonyl Sulphide.

Additional uncertainties were introduced in estimating ΔNEE from ΔGPP. Due to the inherent limitations of remote sensing, which can track GPP but not the total ecosystem respiration (the sum of HR and AR), certain assumptions must be made. First, to estimate AR, we assumed that ΔGPP and ΔNPP can be related through a constant carbon use efficiency (CUE) parameter that varies across vegetation type, age, and management practices (Campioli et al., 2015; DeLucia et al., 2007; Manzoni et al., 2018; Y. He et al., 2018; S. Yu et al., 2023). In our analysis, we adopted a mean value of 0.60 with an uncertainty of range 20% (0.5–0.7), which encompasses most literature estimates. Second, we assumed that the influence of ΔHR on the ΔNEE was negligible. The secondary impact of ΔHR is supported by Yin et al. (2020), who were able to reasonably reproduce observed atmospheric CO_2 enhancements during the 2019 US Midwest floods while neglecting ΔHR variations. Still, it is important to note that HR is sensitive to variations in temperature and moisture. Terrestrial biosphere models could serve as potential tools for estimating ΔHR (e.g., Balashov et al. (2022)) as remote sensing does not adequately capture variations in HR, which is significantly influenced by the availability of labile carbon. However, the accuracy of these model-driven estimates remains challenging to verify.

5 Open Research

Once accepted for publication, the prior and posterior fluxes, TROPOMI-based GPP, and NIR_V-based GPP will be archived with a DOI. During the review processes the data are available by contacting Brendan Byrne. The atmospheric CO_2 inversion analyses performed in this study used the CMS-Flux model, which is based on the GEOS-Chem Adjoint model that can be accessed from the GEOS-Chem Wiki (https://wiki.seas.harvard.edu/geos-chem). OCO-2 X_{CO_2} Lite files can be downloaded from the GES DISC (https://disc.gsfc.nasa.gov). In Situ CO_2 measurements (Schuldt et al., 2022) can be downloaded from https://gml.noaa.gov/ccgg/obspack/. GFED biomass burning emissions (van der Werf et al., 2017) were downloaded from https://globalfiredata.org/. Fossil fuel emissions (Basu & Nassar, 2021) were downloaded from https://doi.org/10.5281/zenodo.4776925. MERRA-2 reanalysis data (Gelaro et al., 2017) was downloaded from https://disc.gsfc.nasa.gov/. TROPOMI SIF data are accessed online at https://data.caltech.edu/records/1347 (DOI: 10.22002/D1.1347). FluxSat Version 2 (Joiner & Yoshida, 2021) were downloaded from the ORNL DAAC (https://daac.ornl.gov). GOSIF GPP (Li & Xiao, 2019) were downloaded from http://data.globalecology.unh.edu/. FLUXCOM GPP (Jung et al., 2020) was downloaded from the aata portal of the Max Planck Institute for Biogeochemistry (https://www.bgc-jena.mpg.de/geodb/projects/Home.php).

Acknowledgments

The research carried out at the Jet Propulsion Laboratory, California Institute of Technology, was under a contract with the National Aeronautics and Space Administration. Funding for the research was from the NASA CMS (grant nos. 80NSSC21K1060, 80NM0018F0583) and OCO science team (grant np. 80NM0018F0583) programs. Resources supporting this work were provided by the NASA High-End Computing (HEC) program through the NASA Advanced Supercomputing (NAS) Division at Ames Research Center.

References

Balashov, N., Ott, L. E., Weir, B., Basu, S., Davis, K. J., Miles, N. L., … Stauffer, R. M. (2022). Flood impacts on net ecosystem exchange in the midwestern and southern united states in 2019. doi: 10.1002/essoar.10512359.1

Barkhordarian, A., Bowman, K. W., Cressie, N., Jewell, J., & Liu, J. (2021). Emergent constraints on tropical atmospheric aridity—carbon feedbacks and the future of carbon sequestration. *Environmental Research Letters*, *16*(11), 114008.

Basu, S., & Nassar, R. (2021, January). *Fossil Fuel CO Emissions for the OCO2 Model Intercomparison Project (MIP).* Zenodo. Retrieved from `https://doi.org/10.5281/zenodo.4776925` (Previous versions available from (2018): https://g mao.gsfc.nasa.gov/gmaoftp/sourish/ODIAC/2018/distr ib/, (2017): ftp://aftp.cmdl.noaa.gov/data/ccgg/OD IAC/2017/distrib/, (2016): ftp://aftp.cmdl.noaa.go v/data/ccgg/ODIAC/2016/distrib/, (2015a): ftp://af tp.cmdl.noaa.gov/data/ccgg/ODIAC/2015a/distrib/) doi: 10.5281/zenodo.4776925

Byrne, B., Baker, D. F., Basu, S., Bertolacci, M., Bowman, K. W., Carroll, D., … Zeng, N. (2023). National CO_2 budgets (2015–2020) inferred from atmospheric CO_2 observations in support of the global stocktake. *Earth System Science Data*, *15*(2), 963–1004. Retrieved from `https://essd.copernicus.org/articles/15/963/2023/` doi: 10.5194/essd-15-963-2023

Byrne, B., Jones, D. B. A., Strong, K., Polavarapu, S. M., Harper, A. B., Baker, D. F., & Maksyutov, S. (2019). On what scales can gosat flux inversions constrain anomalies in terrestrial ecosystems? *Atmos. Chem. Phys.*, *19*(20), 13017–13035. Retrieved from `https://www.atmos-chem-phys.net/19/13017/2019/` doi: 10.5194/acp-19-13017-2019

Byrne, B., Liu, J., Lee, M., Baker, I. T., Bowman, K. W., Deutscher, N. M., ... Wunch, D. (2020). Improved constraints on northern extratropical CO_2 fluxes obtained by combining surface-based and space-based atmospheric CO_2 measurements. *Journal ofGeophysical Research: Atmospheres*, *125*. doi: 10.1029/2019JD032029

Byrne, B., Liu, J., Lee, M., Yin, Y., Bowman, K. W., Miyazaki, K., ... Paton-Walsh, C. (2021). The carbon cycle of southeast Australia during 2019–2020: Drought, fires, and subsequent recovery. *AGU Advances*, *2*(4), e2021AV000469. doi: 10.1029/2021AV000469

Campioli, M., Vicca, S., Luyssaert, S., Bilcke, J., Ceschia, E., Chapin III, F. S., ... others (2015). Biomass production efficiency controlled by management in temperate and boreal ecosystems. *Nature geoscience*, *8*(11), 843–846.

Chen, H. W., Zhang, F., Lauvaux, T., Davis, K. J., Feng, S., Butler, M. P., & Alley, R. B. (2019). Characterization of regional-scale co2 transport uncertainties in an ensemble with flow-dependent transport errors. *Geophysical Research Letters*, *46*(7), 4049–4058.

Chen, H. W., Zhang, F., Lauvaux, T., Scholze, M., Davis, K. J., & Alley, R. B. (2023). Regional co_2 inversion through ensemble-based simultaneous state and parameter estimation: TRACE framework and controlled experiments. *Journal of Advances in Modeling Earth Systems*, *15*(3), e2022MS003208.

Ciais, P., Reichstein, M., Viovy, N., Granier, A., Ogée, J., Allard, V., ... others (2005). Europe-wide reduction in primary productivity caused by the heat and drought in 2003. *Nature*, *437*(7058), 529–533. doi: https://doi.org/10.1038/nature03972

Davis, K. J., Browell, E. V., Feng, S., Lauvaux, T., Obland, M. D., Pal, S., ... others (2021). The atmospheric carbon and transport (act)-america mission. *Bulletin of the American Meteorological Society*, *102*(9), E1714–E1734.

Davis, K. J., Obland, M., Lin, B., Lauvaux, T., O'Dell, C., Meadows, B., ... Pauly, R. (2018). *ACT-America: L3 merged in situ atmospheric trace gases and flask data, eastern usa.* ORNL Distributed Active Archive Center. Retrieved from `https://daac.ornl.gov/cgi-bin/dsviewer.pl?ds_id=1593` doi: 10.3334/ORNLDAAC/1593

DeLucia, E., Drake, J. E., Thomas, R. B., & Gonzalez-Meler, M. (2007). Forest carbon use efficiency: is respiration a constant fraction of gross primary production? *Glob. Change Biol.*, *13*(6), 1157–1167.

Fargione, J. E., Bassett, S., Boucher, T., Bridgham, S. D., Conant, R. T., Cook-Patton, S. C., ... others (2018). Natural climate solutions for the United States. *Science Advances*, *4*(11), eaat1869.

Feldman, A. F., Zhang, Z., Yoshida, Y., Chatterjee, A., & Poulter, B. (2023). Using Orbiting Carbon Observatory-2 (OCO-2) column CO_2 retrievals to rapidly detect and estimate biospheric surface carbon flux anomalies. *Atmospheric Chemistry and Physics*, *23*(2), 1545–1563. Retrieved from `https://acp.copernicus.org/articles/23/1545/2023/` doi: 10.5194/acp-23-1545-2023

Feng, S., Lauvaux, T., Davis, K. J., Keller, K., Zhou, Y., Williams, C., ... Baker, I. (2019). Seasonal characteristics of model uncertainties from biogenic fluxes, transport, and large-scale boundary inflow in atmospheric co_2 simulations over north america. *J. Geophys. Res.-Atmos.*, *124*(24), 14325–14346. doi: 10.1029/2019JD031165

Feng, S., Lauvaux, T., Keller, K., Davis, K. J., Rayner, P., Oda, T., & Gurney, K. R. (2019). A road map for improving the treatment of uncertainties in high-resolution regional carbon flux inverse estimates. *Geophysical Research Letters*, *46*(22), 13461–13469.

Gelaro, R., McCarty, W., Suárez, M. J., Todling, R., Molod, A., Takacs, L., ... others (2017). The modern-era retrospective analysis for research and applications, version 2 (MERRA-2). *J. Climate*, *30*(14), 5419–5454.

Hall, B. D., Crotwell, A. M., Kitzis, D. R., Mefford, T., Miller, B. R., Schibig, M. F., & Tans, P. P. (2021). Revision of the World Meteorological Organization Global Atmosphere Watch (WMO/GAW) CO_2 calibration scale. *Atmospheric Measurement Techniques*, *14*(4), 3015–3032. Retrieved from https://amt.copernicus.org/articles/14/3015/2021/ doi: 10.5194/amt-14-3015-2021

He, L., Byrne, B., Yin, Y., Liu, J., & Frankenberg, C. (2022). Remote-sensing derived trends in gross primary production explain increases in the CO_2 seasonal cycle amplitude. *Global Biogeochemical Cycles*, *36*(9), e2021GB007220. doi: 10.1029/2021GB007220

He, W., Jiang, F., Ju, W., Byrne, B., Xiao, J., Nguyen, N. T., ... others (2023). Do state-of-the-art atmospheric co2 inverse models capture drought impacts on the european land carbon uptake? *Journal of Advances in Modeling Earth Systems*, *15*(6), e2022MS003150.

He, Y., Piao, S., Li, X., Chen, A., & Qin, D. (2018). Global patterns of vegetation carbon use efficiency and their climate drivers deduced from MODIS satellite data and process-based models. *Agricultural and Forest Meteorology*, *256-257*, 150-158. Retrieved from https://www.sciencedirect.com/science/article/pii/S0168192318300923 doi: https://doi.org/10.1016/j.agrformet.2018.03.009

Hu, L., Andrews, A. E., Thoning, K. W., Sweeney, C., Miller, J. B., Michalak, A. M., ... van der Velde, I. R. (2019). Enhanced North American carbon uptake associated with El Niño. *Science advances*, *5*(6), eaaw0076. doi: 10.1126/sciadv.aaw0076

Joiner, J., & Yoshida, Y. (2020). Satellite-based reflectances capture large fraction of variability in global gross primary production (GPP) at weekly time scales. *Agricultural and Forest Meteorology*, *291*, 108092. Retrieved from https://www.sciencedirect.com/science/article/pii/S0168192320301945 doi: https://doi.org/10.1016/j.agrformet.2020.108092

Joiner, J., & Yoshida, Y. (2021). *Global modis and fluxnet-derived daily gross primary production, v2.* ORNL DAAC, Oak Ridge, Tennessee, USA. doi: 10.3334/ORNLDAAC/1835

Jung, M., Schwalm, C., Migliavacca, M., Walther, S., Camps-Valls, G., Koirala, S., ... Reichstein, M. (2020). Scaling carbon fluxes from eddy covariance sites to globe: synthesis and evaluation of the FLUXCOM approach. *Biogeosciences*, *17*(5), 1343–1365. Retrieved from https://www.biogeosciences.net/17/1343/2020/ doi: 10.5194/bg-17-1343-2020

Kim, J., Polavarapu, S. M., Jones, D. B., Chan, D., & Neish, M. (2021). The resolvable scales of regional-scale co2 transport in the context of imperfect meteorology: The predictability of co2 in a limited-area model. *Journal of Geophysical Research: Atmospheres*, *126*(20), e2021JD034896.

Kirchmeier-Young, M. C., & Zhang, X. (2020). Human influence has intensified extreme precipitation in North America. *Proceedings of the National Academy of Sciences*, *117*(24), 13308-13313. Retrieved from https://www.pnas.org/doi/abs/10.1073/pnas.1921628117 doi: 10.1073/pnas.1921628117

Lauvaux, T., Schuh, A. E., Uliasz, M., Richardson, S., Miles, N., Andrews, A. E., ... Davis, K. J. (2012). Constraining the co_2 budget of the corn belt: exploring uncertainties from the assumptions in a mesoscale inverse system. *Atmospheric Chemistry and Physics*, *12*(1), 337–354. Retrieved from https://acp.copernicus.org/articles/12/337/2012/ doi: 10.5194/acp-12-337-2012

Li, X., & Xiao, J. (2019). Mapping photosynthesis solely from solar-induced chlorophyll fluorescence: A global, fine-resolution dataset of gross primary production derived from OCO-2. *Remote Sensing*, *11*(21), 2563.

Li, X., Xiao, J., He, B., Altaf Arain, M., Beringer, J., Desai, A. R., ... others (2018). Solar-induced chlorophyll fluorescence is strongly correlated with terrestrial photosynthesis for a wide variety of biomes: First global analysis based on OCO-2 and flux tower observations. *Global change biology*, *24* (9), 3990–4008.

Liu, J., Bowman, K. W., & Henze, D. K. (2015). Source-receptor relationships of column-average CO_2 and implications for the impact of observations on flux inversions. *J. Geophys. Res.-Atmos.*, *120* (10), 5214–5236. doi: 10.1002/2014JD022914

Liu, J., Bowman, K. W., Schimel, D. S., Parazoo, N. C., Jiang, Z., Lee, M., ... Eldering, A. (2017). Contrasting carbon cycle responses of the tropical continents to the 2015–2016 El Niño. *Science*, *358* (6360). Retrieved from http://science.sciencemag.org/content/358/6360/eaam5690 doi: 10.1126/science.aam5690

Manzoni, S., Čapek, P., Porada, P., Thurner, M., Winterdahl, M., Beer, C., ... Way, D. (2018). Reviews and syntheses: Carbon use efficiency from organisms to ecosystems – definitions, theories, and empirical evidence. *Biogeosciences*, *15* (19), 5929–5949. Retrieved from https://bg.copernicus.org/articles/15/5929/2018/ doi: 10.5194/bg-15-5929-2018

Monteil, G., Broquet, G., Scholze, M., Lang, M., Karstens, U., Gerbig, C., ... Walton, E. M. (2020). The regional european atmospheric transport inversion comparison, eurocom: first results on european-wide terrestrial carbon fluxes for the period 2006–2015. *Atmospheric Chemistry and Physics*, *20* (20), 12063–12091. Retrieved from https://acp.copernicus.org/articles/20/12063/2020/ doi: 10.5194/acp-20-12063-2020

Munassar, S., Monteil, G., Scholze, M., Karstens, U., Rödenbeck, C., Koch, F.-T., ... Gerbig, C. (2023). Why do inverse models disagree? a case study with two european co 2 inversions. *Atmospheric Chemistry and Physics*, *23* (4), 2813–2828.

Munassar, S., Rödenbeck, C., Koch, F.-T., Totsche, K. U., Gałkowski, M., Walther, S., & Gerbig, C. (2022). Net ecosystem exchange (nee) estimates 2006–2019 over europe from a pre-operational ensemble-inversion system. *Atmospheric Chemistry and Physics*, *22* (12), 7875–7892. Retrieved from https://acp.copernicus.org/articles/22/7875/2022/ doi: 10.5194/acp-22-7875-2022

NOAA. (2021, July). *ETOPO 2022 15 Arc-Second Global Relief Model.* NOAA National Centers for Environmental Information. Retrieved from https://doi.org/10.25921/fd45-gt74 doi: 10.25921/fd45-gt74

O'Dell, C. W., Eldering, A., Wennberg, P. O., Crisp, D., Gunson, M. R., Fisher, B., ... Velazco, V. A. (2018). Improved retrievals of carbon dioxide from orbiting carbon observatory-2 with the version 8 acos algorithm. *Atmos. Meas. Tech.*, *11* (12), 6539–6576. Retrieved from https://www.atmos-meas-tech.net/11/6539/2018/ doi: 10.5194/amt-11-6539-2018

Ogle, S. M., Davis, K., Lauvaux, T., Schuh, A., Cooley, D., West, T. O., ... Denning, A. S. (2015, mar). An approach for verifying biogenic greenhouse gas emissions inventories with atmospheric CO_2 concentration data. *Environmental Research Letters*, *10* (3), 034012. Retrieved from https://dx.doi.org/10.1088/1748-9326/10/3/034012 doi: 10.1088/1748-9326/10/3/034012

Schuldt, K. N., Mund, J., Luijkx, I. T., Aalto, T., Abshire, J. B., Aikin, K., ... van den Bulk, P. (2022). *Multi-laboratory compilation of atmospheric carbon dioxide data for the period 1957-2021; obspack_co2_1_globalviewplus_v8.0_2022-08-27.* NOAA Global Monitoring Laboratory. doi: 10.25925/20220808

Seneviratne, S., Zhang, X., Adnan, M., Badi, W., Dereczynski, C., Di Luca, A., ... Zhou, B. (2021). [Book Section]. In V. Masson-Delmotte et al. (Eds.), *Climate change 2021: The physical science basis. contribution of working group i to* *the sixth assessment report of the intergovernmental panel on climate change* (chap. Weather and Climate Extreme Events in a Changing Climate). Cambridge University Press, Cambridge, United Kingdom and New York, NY, USA: Cambridge University Press. doi: 10.1017/9781009157896.013

Shenoy, S., Gorinevsky, D., Trenberth, K. E., & Chu, S. (2022). Trends of extreme US weather events in the changing climate. *Proceedings of the National Academy of Sciences*, *119*(47), e2207536119. Retrieved from `https://www.pnas.org/doi/abs/10.1073/pnas.2207536119` doi: 10.1073/pnas.2207536119

Stanevich, I., Jones, D. B. A., Strong, K., Parker, R. J., Boesch, H., Wunch, D., … Deng, F. (2020). Characterizing model errors in chemical transport modeling of methane: impact of model resolution in versions v9-02 of geos-chem and v35j of its adjoint model. *Geosci. Model Dev.*, *13*(9), 3839–3862. Retrieved from `https://gmd.copernicus.org/articles/13/3839/2020/` doi: 10.5194/gmd-13-3839-2020

Sun, Q., Zhang, X., Zwiers, F., Westra, S., & Alexander, L. V. (2021). A global, continental, and regional analysis of changes in extreme precipitation. *Journal of Climate*, *34*(1), 243 - 258. Retrieved from `https://journals.ametsoc.org/view/journals/clim/34/1/jcliD190892.xml` doi: 10.1175/JCLI-D-19-0892.1

Sun, Y., Frankenberg, C., Wood, J. D., Schimel, D., Jung, M., Guanter, L., … others (2017). OCO–2 advances photosynthesis observation from space via solar-induced chlorophyll fluorescence. *Science*, *358*(6360), eaam5747.

Thompson, R. L., Broquet, G., Gerbig, C., Koch, T., Lang, M., Monteil, G., … others (2020). Changes in net ecosystem exchange over europe during the 2018 drought based on atmospheric observations. *Philosophical Transactions of the Royal Society B*, *375*(1810), 20190512.

Turner, A. J., Köhler, P., Magney, T. S., Frankenberg, C., Fung, I., & Cohen, R. C. (2021). Extreme events driving year-to-year differences in gross primary productivity across the us. *Biogeosciences*, *18*(24), 6579–6588. Retrieved from `https://bg.copernicus.org/articles/18/6579/2021/` doi: 10.5194/bg-18-6579-2021

U.S. Energy Information Administration. (2023). *Energy-related co_2 emission data tables.* `https://www.eia.gov/environment/emissions/state/`. (Accessed 11 Aug 2023)

USDA-NASS. (2020). *Nass - quick stats.* USDA National Agricultural Statistics Service. Washington DC.

van der Werf, G. R., Randerson, J. T., Giglio, L., van Leeuwen, T. T., Chen, Y., Rogers, B. M., … Kasibhatla, P. S. (2017). Global fire emissions estimates during 1997–2016. *Earth Syst. Sci. Data*, *9*(2), 697–720. Retrieved from `https://www.earth-syst-sci-data.net/9/697/2017/` doi: 10.5194/essd-9-697-2017

Wei, Y., Shrestha, R., Pal, S., Gerken, T., Feng, S., McNelis, J., … others (2021). Atmospheric Carbon and Transport–America (ACT-America) data sets: Description, management, and delivery. *Earth and Space Science*, *8*(7), e2020EA001634. doi: 10.1029/2020EA001634

West, T. O., Bandaru, V., Brandt, C. C., Schuh, A. E., & Ogle, S. M. (2011). Regional uptake and release of crop carbon in the united states. *Biogeosciences*, *8*(8), 2037–2046. Retrieved from `https://bg.copernicus.org/articles/8/2037/2011/` doi: 10.5194/bg-8-2037-2011

West, T. O., Brandt, C. C., Baskaran, L. M., Hellwinckel, C. M., Mueller, R., Bernacchi, C. J., … others (2010). Cropland carbon fluxes in the united states: Increasing geospatial resolution of inventory-based carbon accounting. *Ecological Applications*, *20*(4), 1074–1086.

Yin, Y., Byrne, B., Liu, J., Wennberg, P. O., Davis, K. J., Magney, T., … others (2020). Cropland carbon uptake delayed and reduced by 2019 midwest floods. *AGU Advances*, *1*(1), e2019AV000140.

Yu, K., Keller, C. A., Jacob, D. J., Molod, A. M., Eastham, S. D., & Long, M. S. (2018). Errors and improvements in the use of archived meteorological data for chemical transport modeling: an analysis using GEOS-Chem v11-01 driven by GEOS-5 meteorology. *Geosci. Model Dev.*, *11*(1), 305–319. Retrieved from https://www.geosci-model-dev.net/11/305/2018/ doi: 10.5194/gmd-11-305-2018

Yu, S., Falco, N., Patel, N., Wu, Y., & Wainwright, H. (2023, jun). Diverging climate response of corn yield and carbon use efficiency across the U.S. *Environmental Research Letters*, *18*(6), 064049. Retrieved from https://dx.doi.org/10.1088/1748-9326/acd5e4 doi: 10.1088/1748-9326/acd5e4

Zscheischler, J., Westra, S., Hurk, B. J. J. M. v. d., Seneviratne, S. I., Ward, P. J., Pitman, A., … Zhang, X. (2018). Future climate risk from compound events. *Nature Climate Change*, *8*(6), 469–477.

Supporting Information for "Regional inversion shows promise in capturing extreme-event-driven CO_2 flux anomalies but is limited by atmospheric CO_2 observational coverage"

B. Byrne[1], J. Liu[1,2], K. W. Bowman[1,3], Y. Yin[2,*], J. Yun[1], G. D. Ferreira[4],

S. M. Ogle[4,5], L. Baskaran[1], L. He[6], X. Li[7], J. Xiao[8], K. J. Davis[9]

[1]Jet Propulsion Laboratory, California Institute of Technology, Pasadena, CA, USA

[2]Division of Geological and Planetary Sciences, California Institute of Technology, Pasadena, CA, USA

[3]Joint Institute for Regional Earth System Science and Engineering, University of California, Los Angeles, USA

[4]Natural Resource Ecology Laboratory, Colorado State University, Fort Collins, CO 80523, United States of America

[5]Department of Ecosystem Science and Sustainability, Colorado State University, Fort Collins, CO 80523, United States of America

[6]Department of Global Ecology, Carnegie Institution for Science, Stanford, CA, United States of America

[7]Research Institute of Agriculture and Life Sciences, Seoul National University, Seoul, South Korea

[8]Earth Systems Research Center, Institute for the Study of Earth, Oceans, and Space, University of New Hampshire, Durham, NH, USA

[9]Department of Meteorology and Atmospheric Science, and Earth and Environmental Systems Institute, The Pennsylvania State University, University Park, Pennsylvania

[*]Now at Department of Environmental Studies, New York University, New York, NY, USA

Contents of this file

1. Text S1 to S2
2. Figures S1 to S15

Text S1.

This section provides an extended description of the comparison of posterior CO_2 fields with independent aircraft CO_2 measurements. Co-samples were made for all aircraft measurements that were deemed assimilable in version 8.0 of the the NOAA GLOBALVIEW plus Obspack dataset (Schuldt et al., 2022). To simplify the analysis, we examine three regions over North America, shown in Fig. S7. We aggregate temporally to weekly mean obs minus model mismatches within each region, to better match the timescale being optimized in the inversions. Figure S8 shows plots of the obs minus model statistics across all weeks in each region for the boundary layer (<2000 m) and free troposphere (>2000 m), while Figs. S9–S11 show vertical profiles of the obs minus model differences for each week. Overall, we find that both the prior and posterior CO_2 fields show close agreement to independent aircraft CO_2 observations, with differences close to expected representativeness errors. The obs-model mismatches do not show large differences between flux estimates, suggesting that the data-model mismatch has limited sensitivity to flux estimates on the scale optimized (weekly, $4° \times 5°$), and may be largely driven by transport errors and higher spatial and temporal flux variations. Nevertheless, the posterior CO_2 fields generally show smaller mean biases. Overall, the LNLGOGIS experiment shows the smallest biases, suggesting that additional data improves regional flux estimates (despite concerns about the quality of ocean glint data (Byrne et al., 2023)). That said, the obs minus model differences are quite small for all cases.

Finally, we examine the obs minus model differences for ΔNEE-sensitive observations. To find ΔNEE-sensitive observations, we simulate and atmospheric CO_2 pulse using bottom-up ΔNEE for 2018 and 2019, then define any observation with a signal greater than 0.5 ppm to be ΔNEE-sensitive. Figure. S12 shows the obs minus model differences for ΔNEE-sensitive observations during 2018 and 2019. All experiments are found to show close agreement with the observations. Overall, we find that the LNLGOGIS shows a slightly smaller bias than the other experiments.

Text S2.

This section provides an extended description of a set of flux inversions with imposed prior IAV. For these experiments, prior IAV is introduced by imposing year-specific bottom-up NPP estimates (assumed to equal $0.65 \times$ GPP) in the prior, and optimizing climatotlogical HR. Note that the experiments with a climatological prior impose 2018-2019 mean NPP for both years.

Figures S13–S15 show the posterior ΔNEE estimates for the prior with imposed IAV. The spatial structures in IAV correspond closely to both the prior and inversions using climatological priors. However, the magnitude of ΔNEE is generally much increased for both the US Midwest (Fig. S13) and other regions within CONUS (Fig. S15). The increase in magnitude is consistent with OSSEs, suggesting that the climatological priors underestimate the magnitude of the anomalies, however the relative accuracy of these inversions is difficult to quantify.

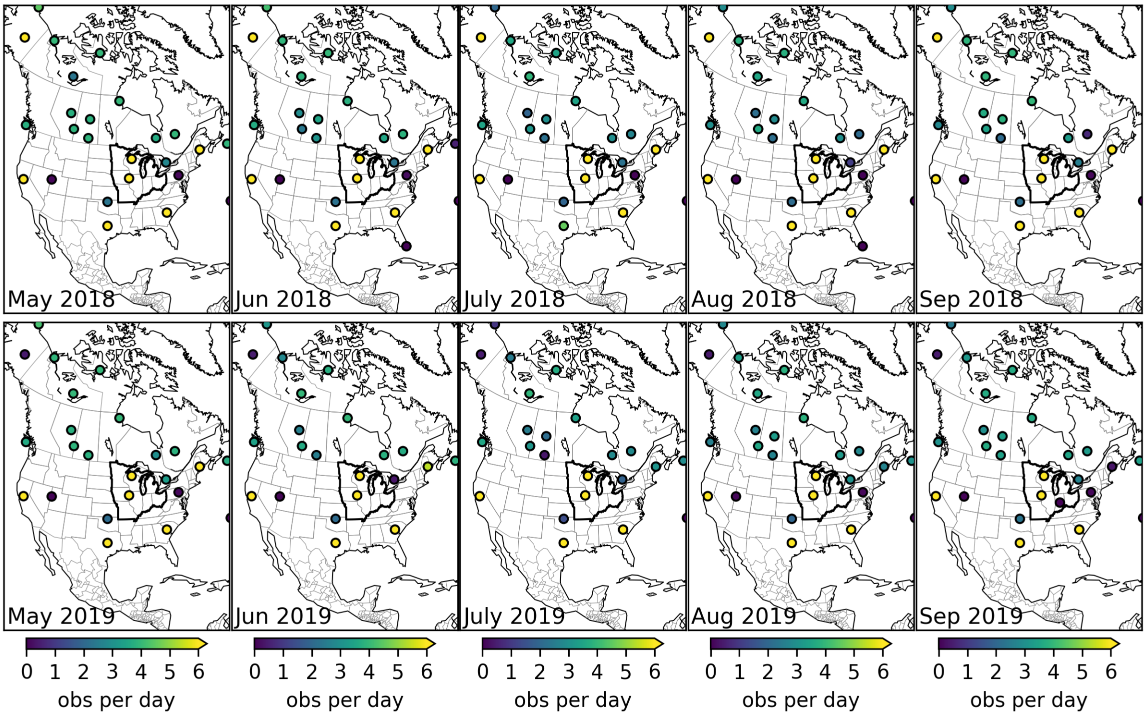

Figure S1. Monthly observational coverage of assimilated in situ measurements over North America for May–Sep during 2018 and 2019. Note that measurements over Canada end in July of 2019.

References

Byrne, B., Baker, D. F., Basu, S., Bertolacci, M., Bowman, K. W., Carroll, D., … Zeng, N. (2023). National CO_2 budgets (2015–2020) inferred from atmospheric CO_2 observations in support of the global stocktake. *Earth System Science Data*, *15*(2), 963–1004. Retrieved from `https://essd.copernicus.org/articles/15/963/2023/` doi: 10.5194/essd-15-963-2023

Schuldt, K. N., Mund, J., Luijkx, I. T., Aalto, T., Abshire, J. B., Aikin, K., … van den Bulk, P. (2022). *Multi-laboratory compilation of atmospheric carbon dioxide data for the period 1957-2021; obspack_co2_1_globalviewplus_v8.0_2022-08-27.* NOAA Global Monitoring Laboratory. doi: 10.25925/20220808

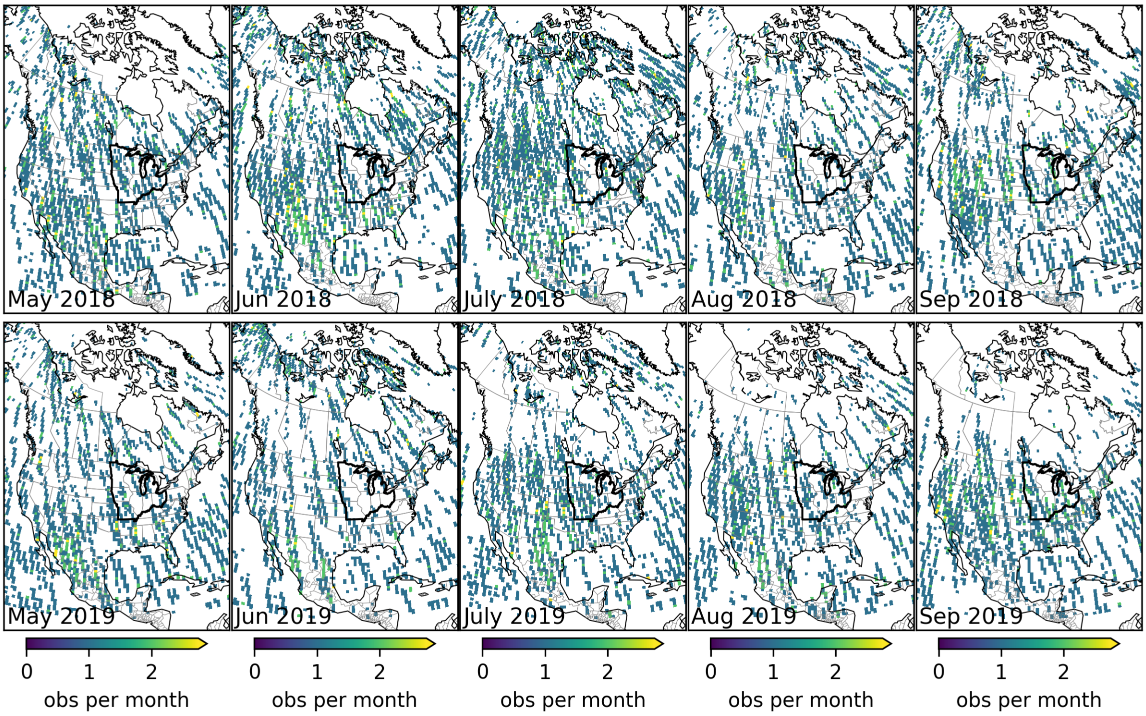

Figure S2. Monthly observational coverage of assimilated OCO-2 X_{CO_2} retrievals over North America for May–Sep during 2018 and 2019.

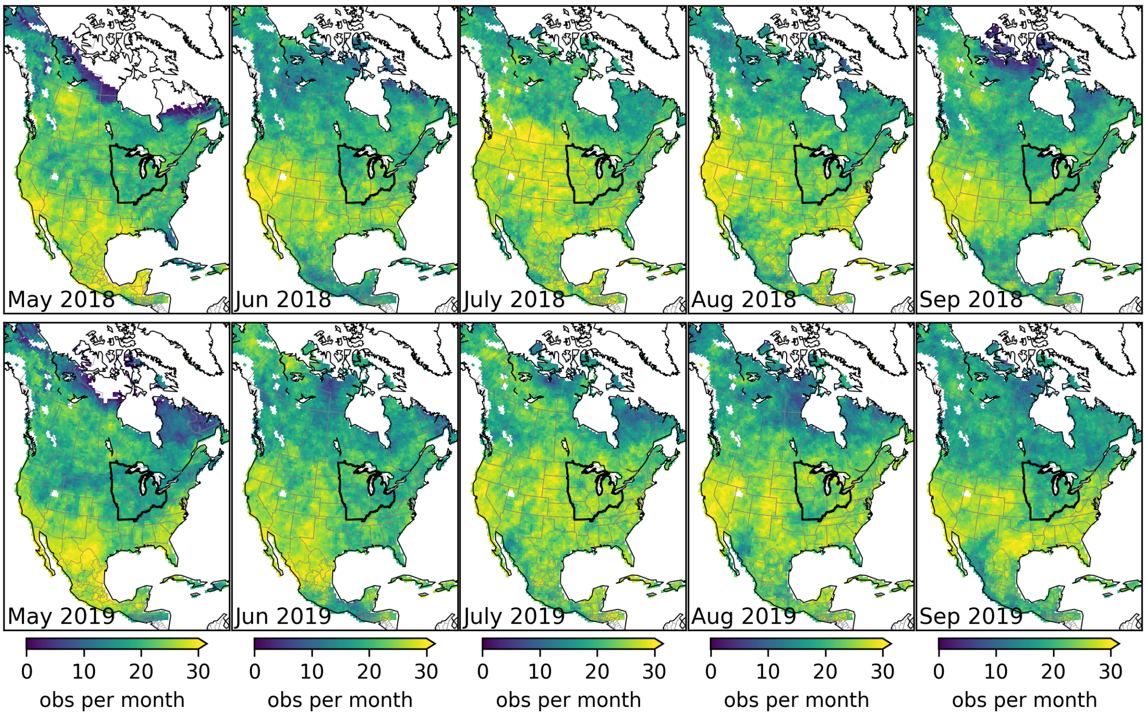

Figure S3. Monthly observational coverage of assimilated ideal LEO pseudo-X_{CO_2} retrievals over North America for May–Sep during 2018 and 2019.

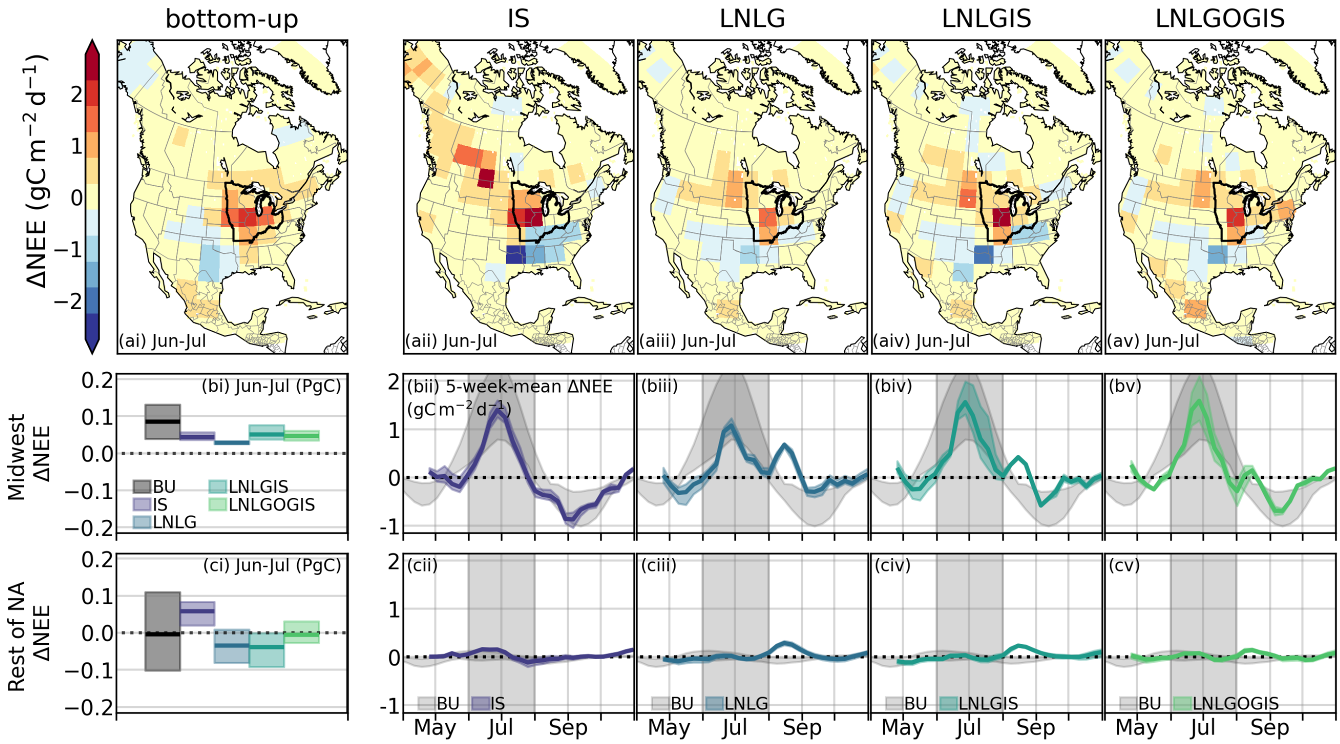

Figure S4. ΔNEE for each one-way nested atmospheric CO_2 inversion experiment. Top row show June-July maps of the mean ΔNEE for each experiment. Second row shows the ΔNEE within the MidWest and across the rest of North America. Bottom row shows the weekly ΔNEE within the MidWest after applying a 5-week running mean.

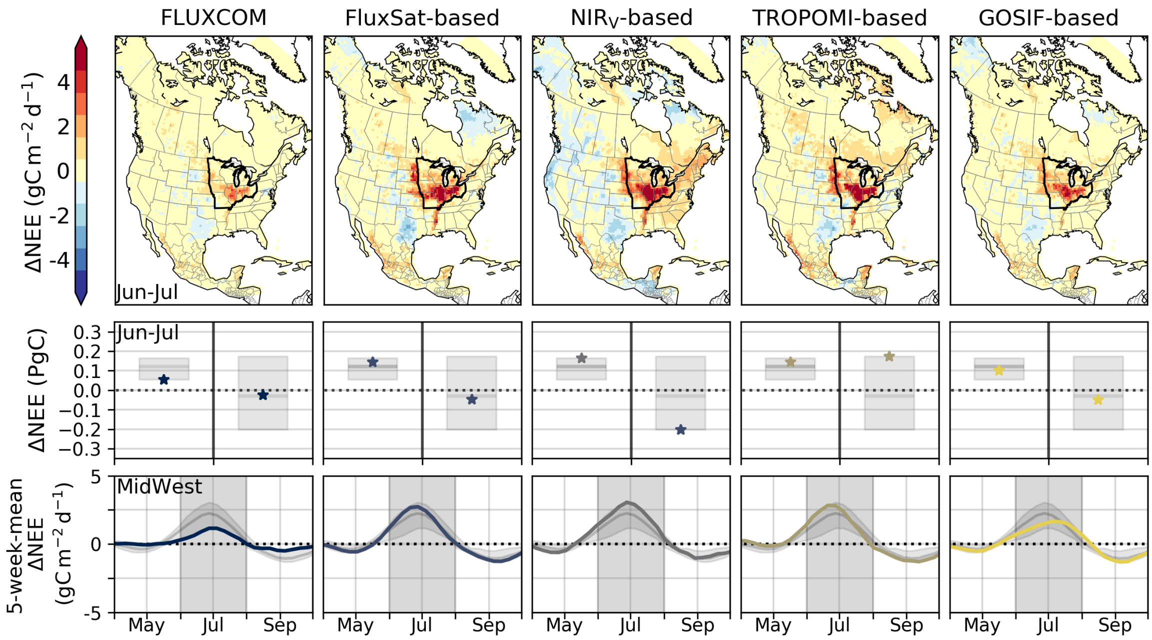

Figure S5. ΔNEE for each bottom-up estimate (best estimate, CUE=0.6). Top row show June–July maps of the mean ΔNEE for each estimate. Second row shows the ΔNEE within the MidWest (on left) and across the rest of North America (on right). Bottom row shows the weekly ΔNEE within the MidWest after applying a 5-week running mean.

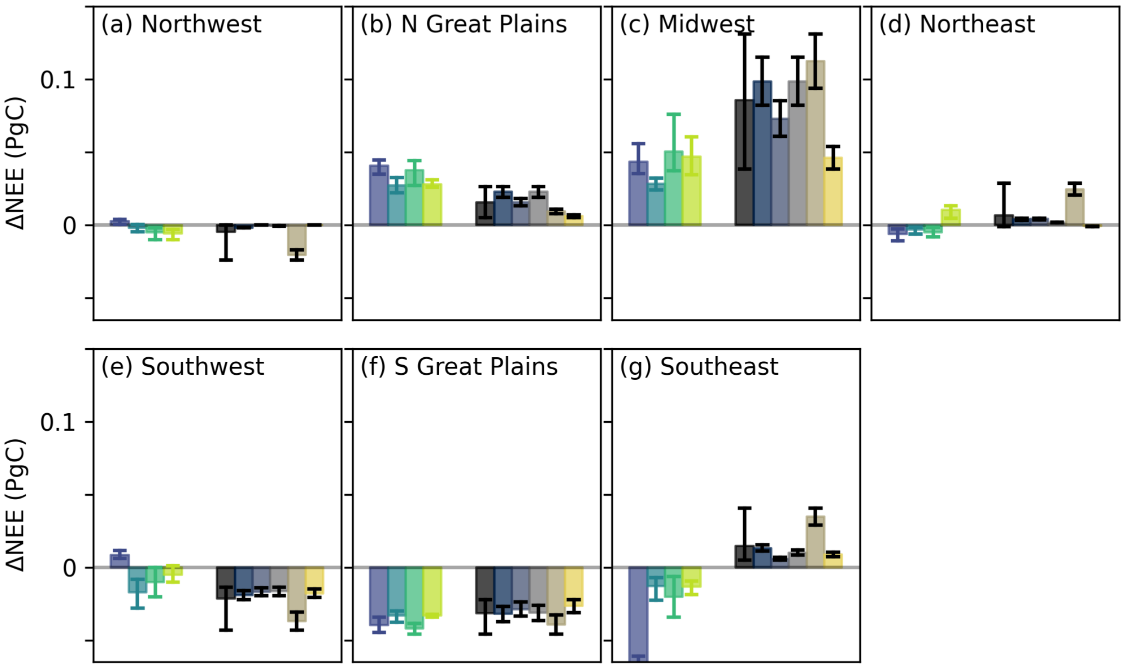

Figure S6. June–July ΔNEE over CONUS National Climate Assessment Regions (https://scenarios.globalchange.gov/regions_nca4).

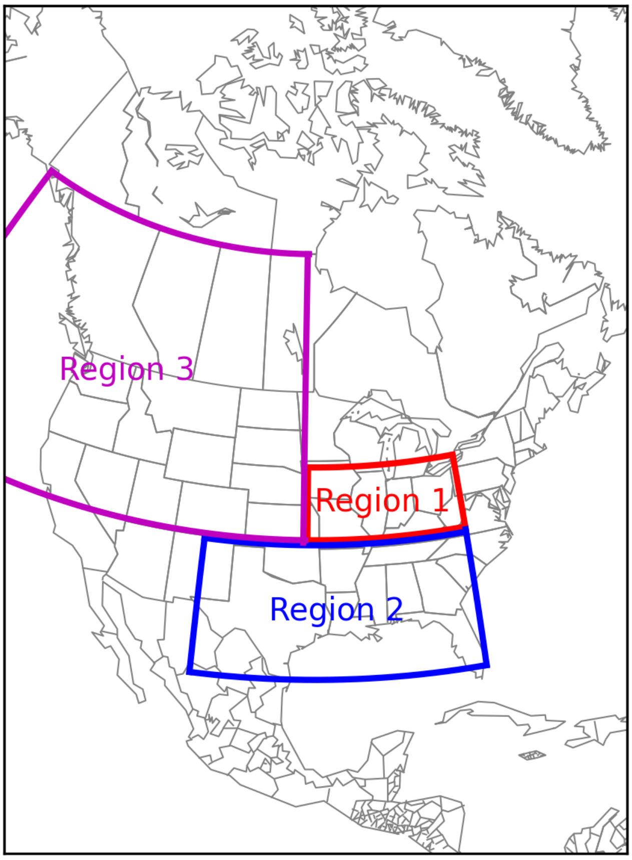

Figure S7. Regions defined for aircraft observation comparisons.

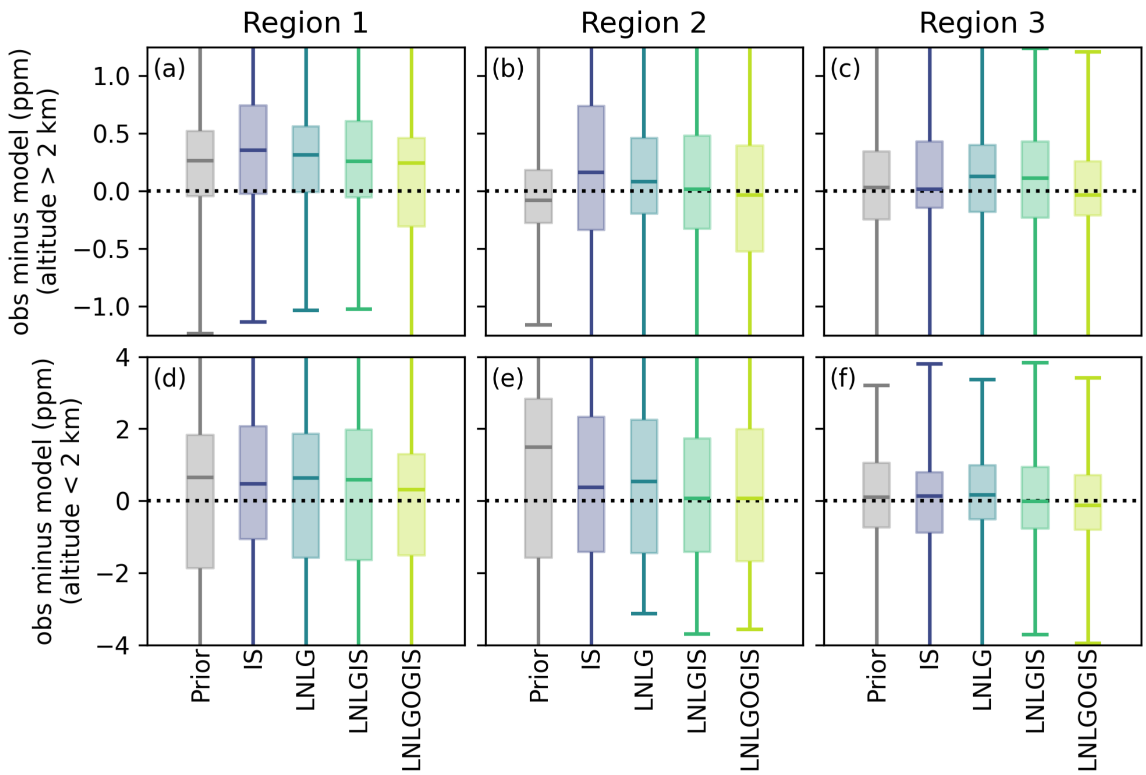

Figure S8. Statistics of weekly obs minus model differences for each region. Differences are shown for both (a-c) the free troposphere and (d-f) the boundary layer. The horizontal line shows the median difference, boxed area shows 25^{th}–75^{th} percentile range and lines show the 0^{th}–100^{th} percentile range.

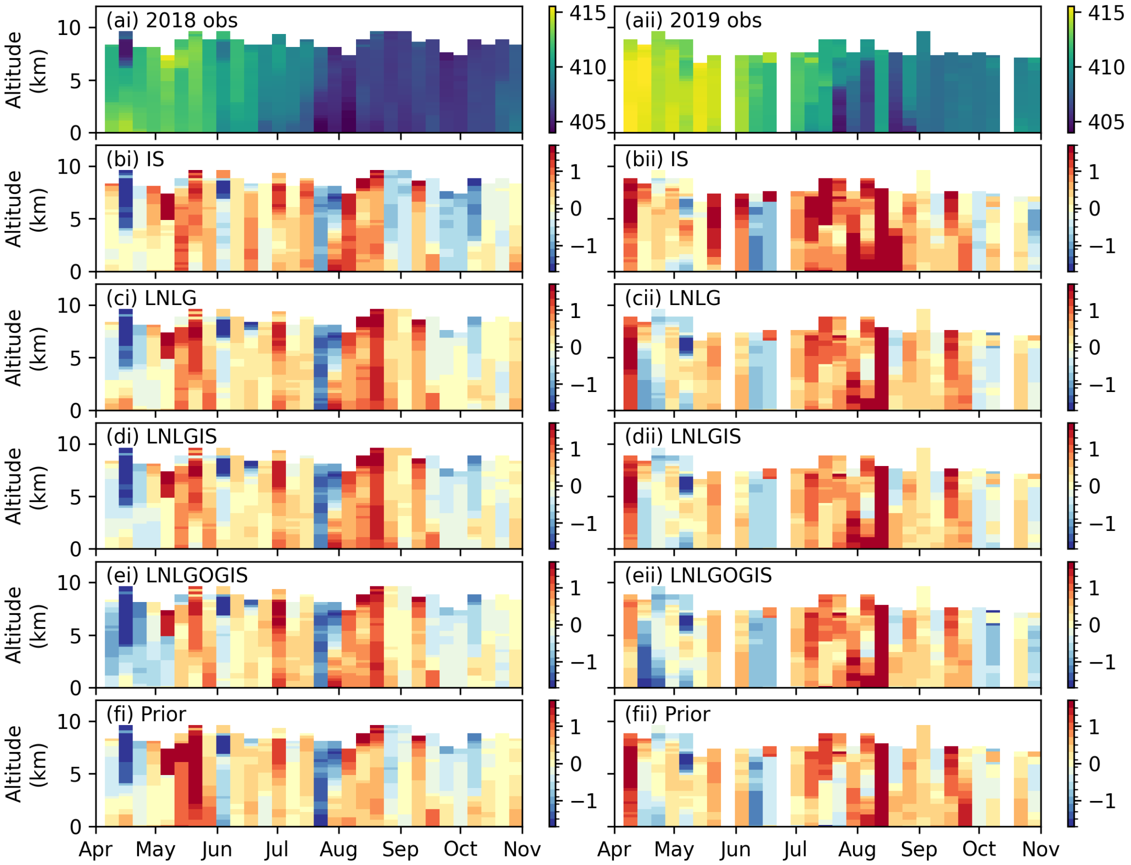

Figure S9. Weekly mean vertical profiles of CO_2 (250 m vertical grid) for all aircraft measurements over Region 1. Aircraft measurements are shown on row (a), with the obs minus model differences shown on the lower rows. Weeks for 2018 and 2019 are shown in columns (i) and (ii), respectively.

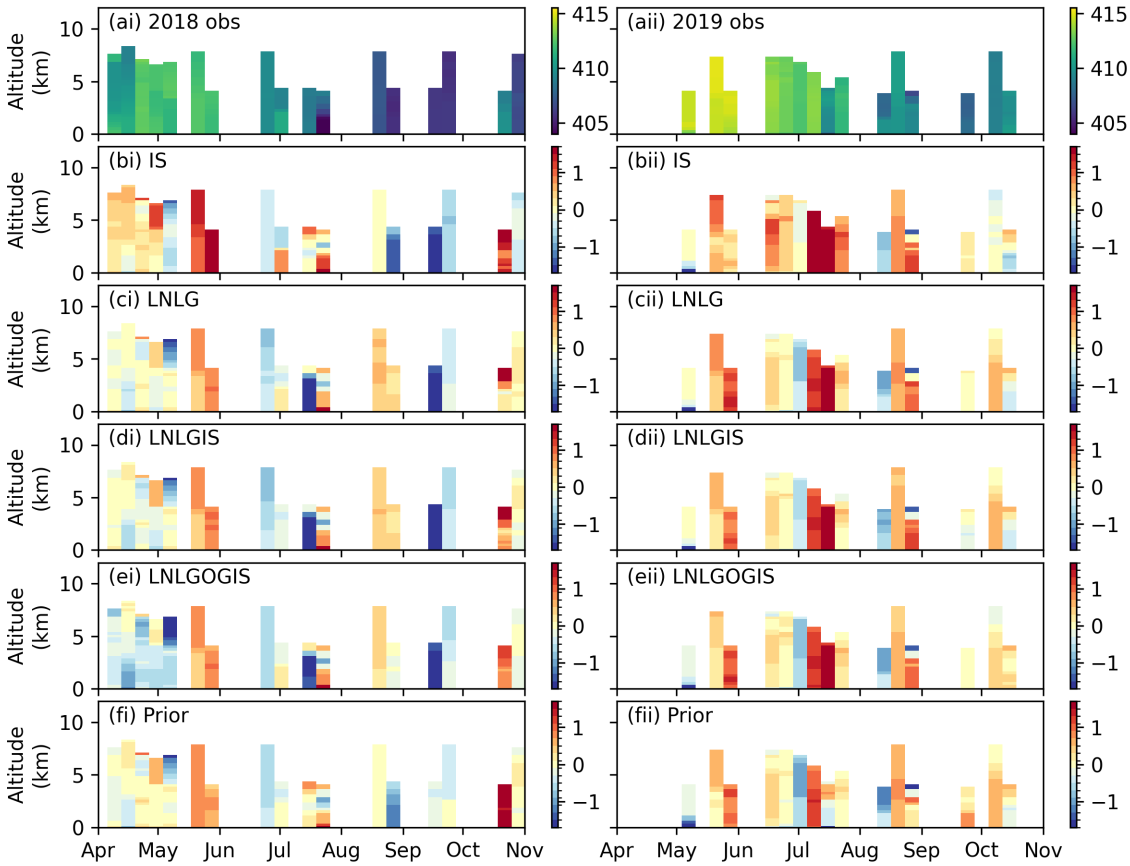

Figure S10. Weekly mean vertical profiles of CO_2 (250 m vertical grid) for all aircraft measurements over Region 2. Aircraft measurements are shown on row (a), with the obs minus model differences shown on the lower rows. Weeks for 2018 and 2019 are shown in columns (i) and (ii), respectively.

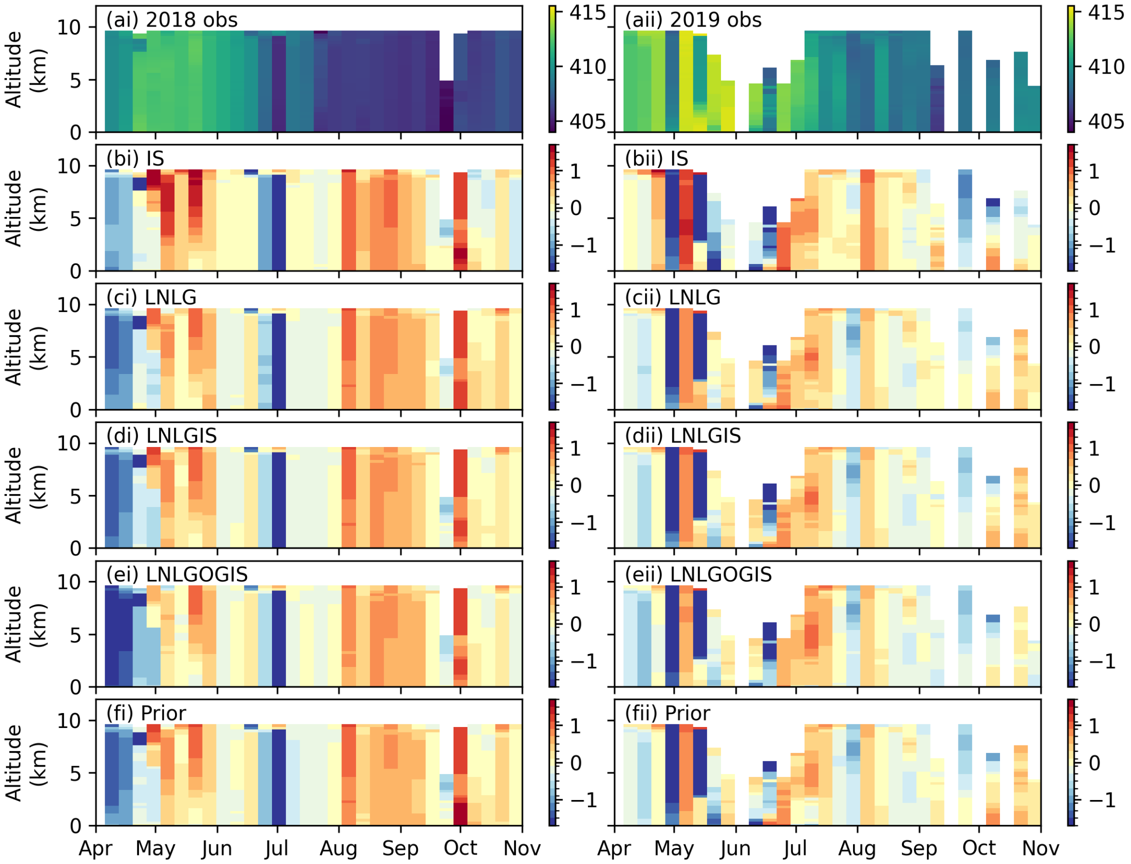

Figure S11. Weekly mean vertical profiles of CO_2 (250 m vertical grid) for all aircraft measurements over Region 3. Aircraft measurements are shown on row (a), with the obs minus model differences shown on the lower rows. Weeks for 2018 and 2019 are shown in columns (i) and (ii), respectively.

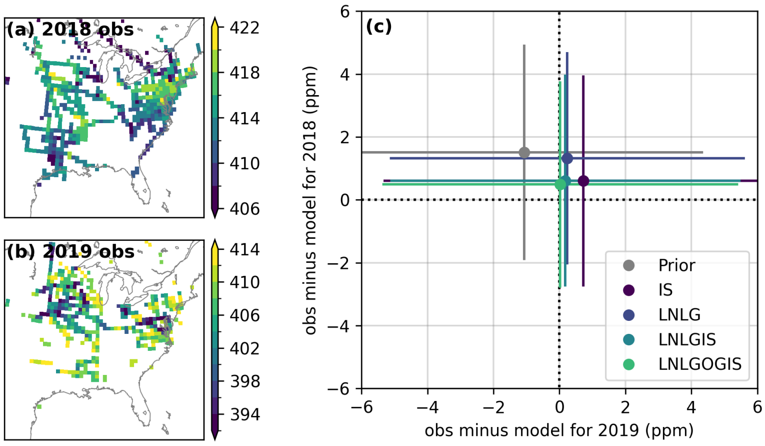

Figure S12. Median plus/minus standard deviation of the obs minus model difference for ΔNEE-sensitive atmospheric CO_2 measurements in 2018 versus 2019 (see Text S1). These statistics are calculated across all individual observations that qualify as flood-sensitive.

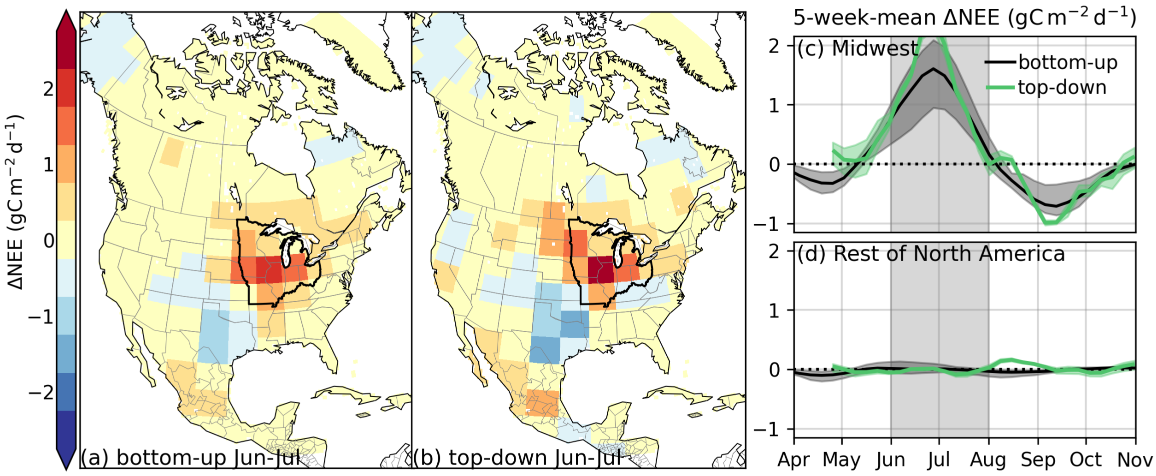

Figure S13. Same as Fig. 1 but for inversions with prior IAV prescribed. (a) Bottom-up and (b) top-down (LNLGOGIS) spatial patterns of June–July mean ΔNEE at 4° × 5° spatial resolution. (c) US Midwest and (d) rest of North America 5-week-mean ΔNEE. The US Midwest is defined as the area within Illinois, Indiana, Iowa, Michigan, Minnesota, Missouri, Ohio, and Wisconsin and is indicated by the black outline in panels (a) and (b).

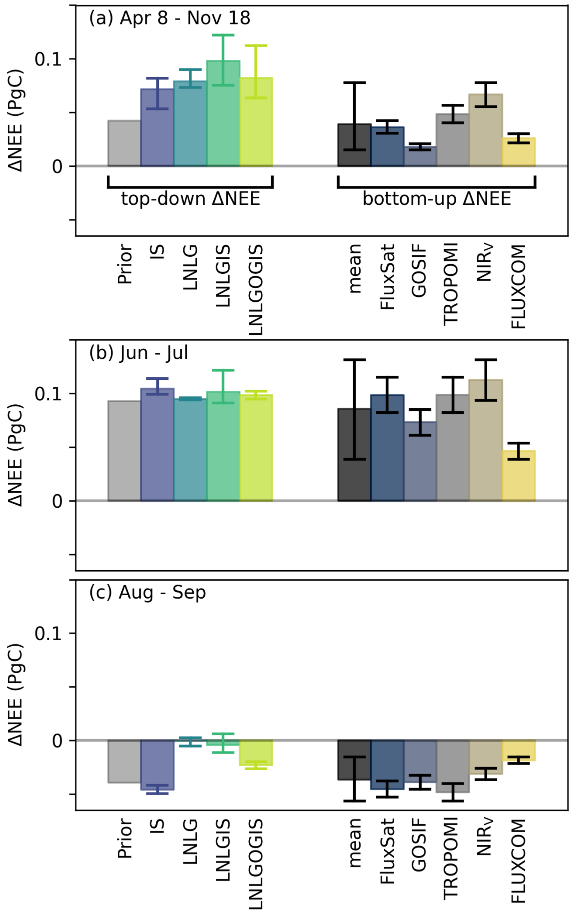

Figure S14. Same as Fig. 2 but for inversions with prior IAV prescribed. Top-down ΔNEE, bottom-up ΔNEE, and yield-based ΔNPP for crops (ΔNPP$_{crop}$) over the US Midwest. ΔNEE is calculated for (a) the entire inversion period (April 8th – Nov 18th), (b) June-July and (c) Aug-Sep. The top-down estimates show the mean and range obtained using three different priors.

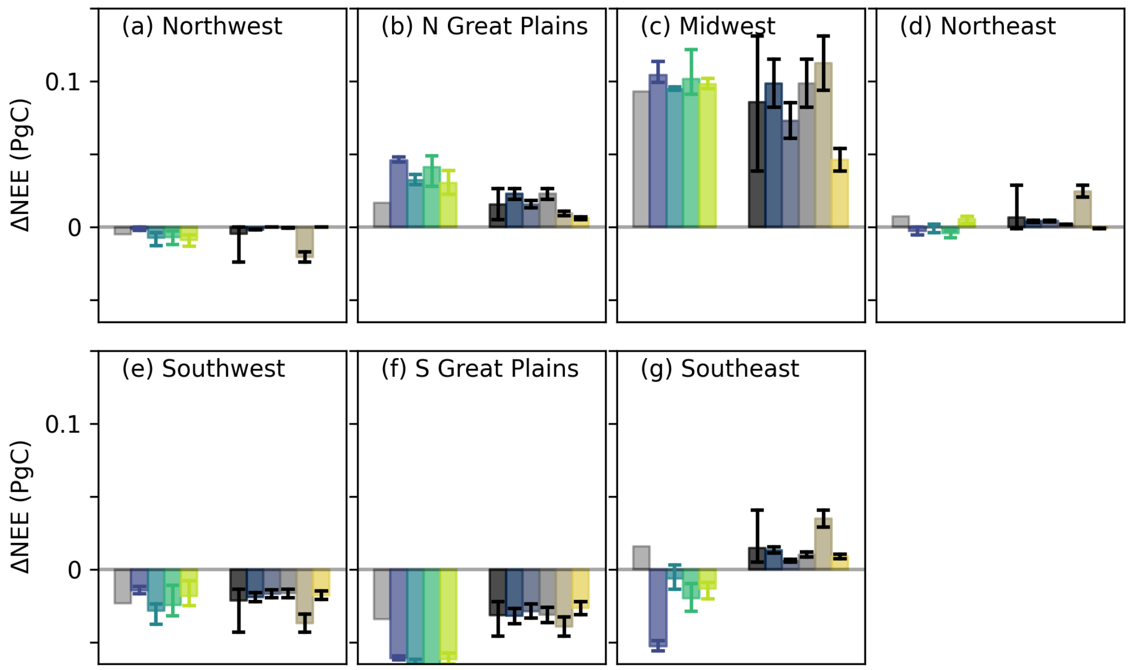

Figure S15. Same as Fig. S6 but for inversions with prior IAV prescribed. June–July ΔNEE over CONUS National Climate Assessment Regions (https://scenarios.globalchange.gov/regions_nca4) for top-down estimates with prior IAV.